# WRF-Chem simulation of aerosol seasonal variability in the San Joaquin Valley

Longtao Wu[1], Hui Su[1], Olga V. Kalashnikova[1], Jonathan H. Jiang[1], Chun Zhao[2], Michael J. Garay[1], James R. Campbell[3] and Nanpeng Yu[4]

*1. Jet Propulsion Laboratory, California Institute of Technology, Pasadena, CA, USA*

*2. School of Earth and Space Sciences, University of Science and Technology of China, Hefei, Anhui, China*

*3. Naval Research Laboratory, Monterey, CA, USA*

*4. University of California, Riverside, Riverside, CA, USA*

Submitted to *Atmospheric Chemistry and Physics*

April, 2017



*Corresponding author address:* Longtao Wu, 4800 Oak Grove Dr., Pasadena, CA 91109
E-mail: Longtao.Wu@jpl.nasa.gov

Highlights:

1. The WRF-Chem simulation successfully captures aerosol variations in the cold season in the San Joaquin Valley (SJV), but has poor performance in the warm season.
2. High resolution model simulation can better resolve inhomogeneous distribution of anthropogenic emissions in urban areas, resulting in better simulation of aerosols in the cold season in the SJV.
3. Observations show that dust is a major component of aerosols in the SJV, especially in the warm season. Poor performance of the WRF-Chem model in the warm season is mainly due to misrepresentation of dust emission and vertical mixing.

## Abstract

WRF-Chem simulations of aerosol seasonal variability in the San Joaquin Valley (SJV), California are evaluated by satellite and in-situ observations. Results show that the WRF-Chem model successfully captures the distribution, magnitude and variation of SJV aerosols during the cold season. However, aerosols are not well represented in the warm season. Aerosol simulations in urban areas during the cold season are sensitive to model horizontal resolution, with better simulations at 4 km resolution than at 20 km resolution, mainly due to inhomogeneous distribution of anthropogenic emissions and better represented precipitation in the 4 km simulation. In rural areas, the model sensitivity to grid size is rather small. Our observational analysis reveals that dust is a primary contributor to aerosols in the SJV, especially during the warm season. Aerosol simulations in the warm season are sensitive to parameterization of dust emission in WRF-Chem. The GOCART (Goddard Global Ozone Chemistry Aerosol Radiation and Transport) dust scheme produces very little dust in the SJV while the DUSTRAN (DUST TRANsport model) scheme overestimates dust emission. Vertical mixing of aerosols is not adequately represented in the model based on CALIPSO (Cloud-Aerosol Lidar and Infrared pathfinder Satellite Observation) aerosol extinction profiles. Improved representation of dust emission and vertical mixing in the boundary layer are needed for better simulations of aerosols during the warm season in the SJV.

# 1. Introduction

The San Joaquin Valley (SJV) in the southern portion of the California Central Valley is surrounded by coastal mountain range to the west and the Sierra Nevada range to the east. With cool wet winters and hot dry summers, the unique natural environment makes SJV one of the most productive agricultural regions in the world (SJV APCD, 2012 and references therein). However, SJV is also one of the most polluted regions in US due to its unique geographical location. Frequent stagnant weather systems are conducive to air pollution formation, while the surrounding mountains block air flow and trap pollutions. Large seasonal and spatial variation of aerosol occurrence and distribution are observed in the SJV. Although significant progress made to improving local air quality in past decades has been achieved through strong emission controls, PM2.5 (particulate matter with diameter $\leq 2.5$ μm) concentrations in the SJV remain well above the national ambient air quality standards (NAAQS) threshold of 12 μg $m^{-3}$ on an annual basis and 35 μg $m^{-3}$ on daily basis, occurring mainly during the cold season. Improved understanding of the aerosol variability and impacts is needed to provide further guidance for emission control strategies in the SJV.

Air quality models are a useful tool to understanding the formation and evolution of aerosols and their impacts on air quality, weather and climate. However, it is quite challenging to accurately simulate aerosol properties (Fast et al., 2014). Fast et al. (2014) summarized the factors contributing to the errors in regional-scale modeling of aerosol properties. They include 1) emission sources; 2) meteorological parameterizations; 3) representation of aerosol chemistry; 4) limited understanding of the formation processes of secondary organic aerosol (SOA); 5) spatial resolution; and 6) boundary conditions.

As one of the advanced regional air quality models available presently to the community, the Weather Research and Forecasting model with Chemistry (WRF-Chem) has been widely used to study aerosols and their impacts on regional air quality, weather and climate (e.g., Misenis and Zhang, 2010; Zhang et al., 2010; Zhao et al., 2010; 2013a, 2013b; 2014; Gao et al., 2011; Wu et al., 2011a, 2011b, 2013; Fast et al., 2012, 2014; Scarino et al., 2014; Tessum et al., 2015; Campbell et al., 2016; Hu et al., 2016). For example, Fast et al. (2014) showed that WRF-Chem simulations at 4 km horizontal resolution captured the observed meteorology and boundary layer structure over California in May and June of 2010 and the spatial and temporal variations of aerosols were reasonably simulated. Aerosol simulations by WRF-Chem are usually sensitive to both local emission and long-range transport of aerosols from the boundary conditions provided by the global Model for Ozone and Related chemical Tracers, version 4 (MOZART-4). With a similar model set-up, Zhao et al. (2013b) conducted a one-year simulation at 12 km horizontal resolution and found that the WRF-Chem model represented the observed seasonal and spatial variation of surface particulate matter (PM) concentration over California. However, underestimation of elemental carbon (EC) and organic matter (OM) were noticed in the model simulation, with weak sensitivity to horizontal resolution.

In this study, we focus on simulating aerosol seasonal variability in the SJV, California using similar model configurations as that used in Zhao et al. (2013b) and Fast et al. (2014). This paper serves as the first step for future investigation of the aerosol impact on regional climate and the water cycle in California. Previous studies have demonstrated that aerosols are better simulated at higher model resolution (Misenis and Zhang et al., 2010; Qian et al., 2010; Stround et al., 2011; Fountoukis et al., 2013). However, most regional climate studies are still performed with coarse model resolutions (on the order of 10 km) due to the availability of computational resources. This

study will investigate the sensitivity of aerosol simulations to horizontal resolution and identify optimal model physical choices for reasonable representation of aerosol variabilities in the SJV.

Another application of air quality modeling is to provide initial *a priori* fields for remote sensing retrievals. The WRF-Chem model has been proposed as an input for retrieval algorithms to be developed for the recently-selected NASA (National Aeronautics and Space Administration) MAIA (Multi-Angle Imager for Aerosols) mission, which aims to map PM component concentrations in major urban areas (including the SJV, a testbed for the MAIA retrieval algorithm development). A significant challenge for aerosol remote sensing in retrieving spatial information on specific aerosol types, especially near the surface, is caused by the lack of information on the vertical distribution of aerosols in the atmospheric column and limited instrument sensitivity to aerosol types over land. The WRF-Chem model will be used to provide near-real-time estimation of particle properties, aerosol layer heights, and aerosol optical depths (AOD) to constrain the instrument-based PM retrievals. A reasonable estimate of aerosol properties from WRF-Chem is critical to ensuring retrieval speed and quality. Considering the sensitivity of WRF-Chem simulations to various factors such as initial and boundary conditions, model parameterizations and emission sources (e.g., Wu and Petty, 2010; Zhao et al., 2010, 2013a, 2013b; Wu et al., 2011a, 2015; Fast et al., 2014; Campbell et al., 2016; Morabito et al., 2016), careful model evaluations are needed before the simulations can be used operationally for remote sensing retrievals. Thus, this study is important for the development of MAIA retrieval algorithms, critical to the success of the MAIA mission.

This paper is organized as follows. Section 2 describes observational datasets used for model evaluation. Section 3 provides the description of the WRF-Chem model and experiment

setup. Model simulations and their comparison with observations are discussed in section 4. Section 5 presents the conclusions.

# 2. Observations

## 2.1 Column-integrated Aerosol Optical Properties

AOD is a measure of column-integrated light extinction by aerosols and a proxy for total aerosol loading in the atmospheric column. The Aerosol Robotic Network (AERONET) provides ground measurements of AOD every 15 minutes during daytime under clear skies (Holben et al., 1998), with an accuracy approaching ±0.01 (Eck et al., 1999; Holben et al., 2001; Chew et al., 2011). The monthly level 2.0 AOD product with cloud screening and quality control is used in this study. Ångström exponent (AE) is an indicator of aerosol particle size. Small (large) AE values are generally associated with large (small) aerosol particles (Ångström, 1929; Schuster et al., 2006). The AE between 0.4 μm and 0.6 μm is derived from AERONET observed AODs, and is used to evaluate the model-simulated AE. For comparison with simulated AOD, AERONET AOD is interpolated to 0.55 μm from 0.50 μm and 0.675 μm using the AE. In the SJV, only one AERONET station at Fresno, CA (36.79°N, 119.77°W) has regular observations throughout the California water year 2013 (WY2013) from October 2012 to September 2013.

The Multiangle Imaging Spectroradiometer (MISR) (Diner et al., 1998) instrument onboard the Terra satellite has provided global coverage of AOD once a week since December 1999. The standard MISR retrieval algorithm provides AOD observations at 17.6 km resolution using 16x16 pixels of 1.1 km × 1.1 km each. About 70% of MISR AOD retrievals are within 20% of the paired AERONET AOD, and about 50% of MISR AOD falls within 10% of the AERONET AOD, except in dusty and hybrid (smoke+dust) sites (Kahn et al., 2010). We use version 22 of Level 3 monthly AOD product at 0.5° resolution in this study.

## 2.2 Surface Mass Concentration

Surface $PM_{2.5}$ speciation and $PM_{10}$ (particulate matter with diameter $\leq 10$ μm) data are routinely collected by two national chemical speciation monitoring networks: Interagency Monitoring of Protected Visual Environments (IMPROVE) and the $PM_{2.5}$ National Chemical Speciation Network (CSN) operated by Environmental Protection Agency (EPA) (Hand et al. 2011; Solomon et al., 2014). IMPROVE collects 24-h aerosol speciation every third day at mostly rural sites since 1988. The same frequency of aerosol speciation dataset was collected at EPA CSN sites in urban and suburban areas since 2000. The observed organic carbon is converted to OM by multiplying by 1.4 (Zhao et al., 2013b; Hu et al., 2016). Some precursors of aerosol pollutions (such as $NO_2$ and $SO_2$) are observed hourly by EPA (data available at: https://aqsdr1.epa.gov/aqsweb/aqstmp/airdata/download_files.html) and are used in this study. Selected IMPROVE and EPA CSN sites used in this study are shown in Figure 1a.

## 2.3 Aerosol Extinction Profile

The aerosol extinction coefficient profile reflects the attenuation of the light passing through the atmosphere due to the scattering and absorption by aerosol particles as a function of range. Version 3 Level 2 532 nm aerosol extinction profiles derived from Cloud-Aerosol Lidar with Orthogonal Polarization (CALIOP) backscatter profiles collected onboard the Cloud-Aerosol Lidar and Infrared pathfinder Satellite Observation (CALIPSO) satellite are used (Omar et al., 2009; Young and Vaughan, 2009). Seasonal mean profiles are derived for WY2013 based on the methodology outlined in Campbell et al. (2012), whereby quality-assurance protocols are applied to individual profiles before aggregating and averaging the data. We highlight that no individual profiles are included in the averages if the CALIOP Level 2 retrieval failed to resolve any extinction within the column, a potential issue to create bias that has recently been described by

158 Toth et al. (2017). Level 2 532 nm aerosol extinction data classify aerosols into 6 types: clean
159 marine, dust, polluted continental, clean continental, polluted dust and smoke. Dust and polluted
160 dust are distinguished in the averages in this study for their contribution to total extinction and the
161 vertical profile seasonally in the SJV.

162 **2.4 Meteorology**

163 AIRS (Atmospheric Infrared Sounder) onboard the Aqua satellite (Susskind et al., 2003;
164 Divakarla et al., 2006) has provided global coverage of the tropospheric temperature and moisture
165 at approximately 01:30 and 13:30 local time since 2002. AIRS retrievals have root-mean-squared
166 (RMS) error of ~1 K for temperature and ~15% for water vapor (Divakarla et al., 2006). Level 3
167 monthly temperature and moisture retrievals (version 6) at 1° × 1° grid are used in this study.
168 Vertical gradient of equivalent potential temperature ($\theta_e$) marks atmospheric stability and is
169 computed from temperature and moisture profiles observed by AIRS. Vertical profiles from the
170 European Center for Medium-Range Weather Forecasts Interim Re-Analysis (ERA-Interim; Dee
171 et al., 2011) are also used for comparison. Surface observations, including air temperature, relative
172 humidity (RH) and wind speed, are routinely collected at the California Irrigation Management
173 Information System (CIMIS; http://www.cimis.water.ca.gov/). Precipitation used in this study is
174 the Climate Prediction Center (CPC) Unified Gauge-Based Analysis of Daily Precipitation product
175 at 0.25° x 0.25° resolution.

176 ## 3. Model Description and Experiment Setup

177 The WRF-Chem model Version 3.5.1 (Grell et al., 2005) updated by Pacific Northwest
178 National Laboratory (PNNL) is used in this study (Zhao et al., 2014). This study uses the CBM-Z
179 (carbon bond mechanism) photochemical mechanism (Zaveri and Peters, 1999) coupled with the
180 sectional-bin MOSAIC (Model for Simulating Aerosol Interactions and Chemistry) aerosol

scheme (Zaveri et al., 2008) as the chemical driver. The major components of aerosols (nitrate, ammonium, EC, primary OM, sulfate, sea salt, dust, water and other inorganic matter) as well as their physical and chemical processes are simulated in the model. For computational efficiency, aerosol particles in this study are partitioned into four-sectional bins with dry diameter within 0.039-0.156 μm, 0.156-0.625 μm, 0.625-2.5 μm, and 2.5-10.0 μm. Zhao et al. (2013a) compared the impact of aerosol size partition on dust simulations. It showed that the 4-bin approach reasonably produces dust mass loading and AOD compared with the 8-bin approach. The size distribution of the 4-bin approach follows that of the 8-bin approach with coarser resolution, resulting in ±5% difference on the ratio of $PM_{2.5}$-dust/$PM_{10}$-dust in dusty regions (more large particles and less small particles). Dust number loading and absorptivity are biased high in the 4-bin approach compared with the 8-bin approach.

Aerosols are considered to be spherical and internally mixed in each bin (Barnard et al., 2006; Zhao et al., 2013b). The bulk refractive index for each particle is calculated by volume averaging in each bin. Mie calculations as described by Ghan et al. (2001) are used to derive aerosol optical properties (such as extinction, single-scattering albedo, and the asymmetry parameter for scattering) as a function of wavelength. Aerosol radiation interaction is included in the shortwave and longwave radiation schemes (Fast et al., 2006; Zhao et al., 2011). By linking simulated cloud droplet number with shortwave radiation and microphysics schemes, aerosol cloud interaction is effectively simulated in WRF-Chem (Chapman et al., 2009). Aerosol snow interaction is implemented in this version of WRF-Chem (Zhao et al., 2014) by considering aerosol deposition on snow and the subsequent radiative impacts through the SNICAR (SNow, ICe, and Aerosol Radiative) model (Flanner and Zender, 2005, 2006).

The model simulations start on 1 September 2012 and run continuously for 13 months. With the first month used for the model spin-up, our analysis focuses on WY2013 from October 2012 to September 2013. The model is configured with 40 vertical levels and a model top at 50 hPa. The vertical resolution from the surface to 1 km gradually increases from 28 m to 250 m. The model center is placed at 38°N, 121°W, with 250 × 350 grid points at 4 km horizontal resolution (referred to as "4km" hereafter; Table 1), covering California and the surrounding area. To test the sensitivity of the aerosol simulations to horizontal resolution, one simulation with the same model settings and domain coverage is conducted at 20 km horizontal resolution (referred to as "20km" hereafter).

The physics parameterizations used in the simulations include the Morrison double-moment microphysics scheme (Morrison et al., 2009), Rapid Radiative Transfer Model for General circulation model (RRTMG) shortwave and longwave radiation schemes (Iacono et al., 2008), Community Land Model (CLM) Version 4 land surface scheme (Lawrence et al., 2011). The Yonsei University (YSU) planetary boundary layer (PBL) scheme (Hong et al., 2006) is used in all of the simulations, except one sensitivity experiment that uses the ACM2 (Asymmetric Convective Model with non-local upward mixing and local downward mixing; Pleim, 2007) PBL scheme (referred to as "20km_P7" hereafter, Table 1). Previous studies showed that both YSU and ACM2 schemes have good performance in simulating boundary layer properties (e.g., Hu et al., 2010; Xie et al., 2012; Cuchiara et al., 2014; Banks and Baldasano, 2016; Banks et al., 2016; Chen et al., 2017). Subgrid convection, convective transport of chemical constituents and aerosols, and wet deposition from subgrid convection are parameterized using the Grell 3D ensemble cumulus scheme (Grell and Devenyi, 2002) in the 20 km simulations while convective processes are resolved in the 4 km simulations. The ERA-Interim reanalysis serves as initial and boundary

meteorological conditions for WRF-Chem. The MOZART-4 global chemical transport model (Emmons et al., 2010) is used for initial and boundary chemical conditions. Fast et al. (2014) found that the MOZART-4 model overestimates aerosols in the free troposphere over California, which is also found in one of our sensitivity experiments ("20km_BC1" in the supplementary). Following Fast et al. (2014), the chemical initial and boundary conditions from MOZART-4 are divided by two in all simulations except 20km_BC1.

Anthropogenic emissions are provided by US EPA 2005 National Emissions Inventory (NEI05), with area-type emissions on a structured 4-km grid and point-type emissions at specific latitude and longitude locations (US EPA, 2010). Nineteen gases (including $SO_2$, NO, $NH_3$ etc.) are emitted, and aerosol emissions include $SO_4$, $NO_3$, EC, organic aerosols, and total $PM_{2.5}$ and $PM_{10}$ masses. Anthropogenic emissions are updated every hour to account for diurnal variability, while its seasonal variation is not considered in the simulations. A sensitivity experiment with 2011 NEI emissions ("20km_NEI11" in the supplementary) does not produce significantly different results from the 2005 NEI emissions. Biogenic emissions are calculated online using the Model of Emissions of Gases and Aerosols from Nature (MEGAN) model (Guenther et al., 2006). Biomass burning emissions are obtained from the Global Fire Emissions Database version 2.1, with eight-day temporal resolution (Randerson et al., 2007) and updated monthly. Sea salt emissions are derived from the PNNL-updated sea salt emission scheme that includes the correction of particles with radius less than 0.2 μm (Gong et al., 2003) and dependence on sea surface temperature (Jaeglé et al., 2011).

Following Zhao et al. (2013b), dust emission is computed from the GOCART (Goddard Global Ozone Chemistry Aerosol Radiation and Transport) dust scheme (Ginoux et al., 2001) in the 20km and 4km simulations. The GOCART dust scheme estimates the dust emission flux $F$ as

$$F = CSs_p u_{10m}^2 (u_{10m} - u_t) \quad , \tag{249}$$

where $C$ is an empirical proportionality constant, $S$ is a source function for potential wind erosion that is derived from 1° × 1° GOCART database (Freitas et al., 2011), $s_p$ is a fraction of each size class dust in emission, $u_{10m}$ is 10-m wind speed and $u_t$ is a threshold speed for dust emission.

As shown later, a significant amount of dust is observed in the SJV, whereas the GOCART dust scheme produces little dust. Two sensitivity experiments at 20 km and 4 km horizontal resolution (hereafter referred to as "20km_D2" and "4km_D2", respectively) are conducted by switching the dust emission scheme to the DUST TRANsport model (DUSTRAN) scheme (Shaw et al., 2008). The DUSTRAN scheme estimates $F$ as

$$F = \alpha C u_*^4 (1 - \frac{f_w u_{*t}}{u_*}) \quad , \tag{258}$$

where $C$ is an empirical proportionality constant, $\alpha$ is the vegetation mask, $u_*$ is the friction velocity, $u_{*t}$ is a threshold friction velocity and $f_w$ is the soil wetness factor. The $C$ value in both GOCART and DUSTRAN is highly tunable for different regions. The original $C$ values, 1.0 μg $s^2$ $m^{-5}$ in GOCART (Ginoux et al., 2001) and $1.0\times10^{-14}$ g $cm^{-6}$ $s^{-3}$ in DUSTRAN (Shaw et al., 2008), are used in this study.

## 4. Model Simulation Results

Shown in Fig. 1a, our model domain includes three urban sites (Fresno, Bakersfield and Modesto) and two rural sites (Pinnacles and Kaiser) where surface measurements of aerosols are available. Because aerosols properties and model performance are similar at all urban sites, our discussion is focused on the results at Fresno and the simulations for other urban sites are provided in the supplementary materials. Model simulations in the rural areas are presented in the last subsection.

### 4.1 Sensitivity to Horizontal Resolution

Figure 1 features daily mean anthropogenic $PM_{2.5}$ emission rates used in the 20km and 4km simulations, respectively. Although both emission rates are derived from the 4 km NEI05 dataset, localized high emission rates with sharp gradients are evident in urban areas from the 4km simulation (Fig. 1b). The 20km simulation exhibits lower emission rates at the urban areas with weaker gradients due to the reapportionment process (Fig. 1a). As precipitation is an important process that removes aerosols, we examine the simulated precipitation for the 20km and 4km runs and find that the 20km simulation produces 51% more precipitation, although the domain averaged precipitation is lower in the 20km run than the 4km run (Fig. 2a).

Consistent with higher emission rates and lower precipitation at Fresno, the 4km run simulates higher AOD than the 20km run in the cold season (October-November-December and January-February-March; OND and JFM in Fig. 3). Averaged over a broad area encompassing Fresno and Bakersfield, the most polluted region in the SJV (red box in Fig. 1a), the AOD is 0.090 in the 4km and 0.073 in the 20km, a 23% difference. Compared to the MISR observations, the 4km simulation reproduces the spatial distribution and magnitude of AOD in the cold season. However, the AOD difference between the 20km and 4km runs is small in the warm season (April-May-June and July-August-September; AMJ and JAS in Fig. 3), and both runs underestimate AOD by ~50% with respect to the MISR observations.

Comparing the point values at Fresno in the 4km and 20km simulations (Fig. 4a), we find similar results: the 4km AOD is closer to the AERONET measurements and is about 23% higher than that in the 20km run during the cold season, while both runs are biased low in AOD during the warm season. The different model sensitivities to horizontal resolution between the cold and warm seasons suggest that the dominant aerosol sources may be different for the two seasons. We will elaborate upon the aerosol composition in the following section. MISR and AERONET

observations display weak seasonal AOD variation in the SJV and at Fresno, respectively, which is not well represented in the 20km and 4km simulations (Fig. 3 and 4a).

Aside from AOD, significant seasonal variability of AE (Fig. 4b) is shown at Fresno. AE exhibits a maximum about 1.50 in January and a minimum of 0.98 in April, suggesting relatively small particles in the winter and large particles in the spring. A relatively large AE value of 1.40 (corresponding to small particles) is observed in July, possibly related to the wild fires in late July in the SJV. WRF-Chem captures the seasonal variability of the AE well, with a correlation of 0.90 in both the 20km and 4km simulations. The magnitude of AE is also approximately simulated in the cold season, with a mean of 1.15 (1.20) in the 20km (4km) runs compared to 1.33 in the observation. However, the simulated AE is underestimated by ~30% in the warm season, indicating that the simulated particle size is biased high during this period.

Significant seasonal variability of $PM_{2.5}$ is observed in the SJV urban areas (Fig. 5a and Supplementary Fig. 4a and 5a). $PM_{2.5}$ at Fresno peaks in January (26.18 μg $m^{-3}$) and reaches a minimum of 7.03 μg $m^{-3}$ in June, with an annual nonattainment value of 12.64 μg $m^{-3}$ (Fig. 5a). Both the 20km and 4km runs approximately capture the observed seasonal variability of $PM_{2.5}$, with a correlation around 0.90 (Table 2). In the cold season, the 4km simulation overestimates $PM_{2.5}$ by 27% while the 20km simulation exhibits a low bias of 19% compared with IMPROVE observations at Fresno (Table 3). The 4km simulation of $PM_{10}$ is in good agreement with IMPROVE in the winter (December, January and February), but has significant low biases of between 30% and 85% in other months (Fig. 5b). The 20km simulation underestimates $PM_{10}$ throughout WY2013.

$PM_{2.5}$ is a mixture of nitrate ($NO_3$), ammonia ($NH_4$), OM, EC, sulfate ($SO_4$), dust and other aerosols. High concentrations of $PM_{2.5}$ are primarily the result of $NO_3$ at Fresno (Fig. 5c). Both

simulations produce the seasonal variability of $NO_3$ with a correlation of 0.94, but high bias of 17% (75%) is found in the 20km (4km) simulations during the cold season. As one precursor of $NO_3$, $NO_2$ is underestimated by 43% in the 20km run (Fig. 6a). The overestimation in $NO_3$ and underestimation in $NO_2$ suggest that the precursor emissions may not the reason for the high biases in $NO_3$. $NH_4$ shows a similar performance to $NO_3$, with an overestimation by 38% (111%) in the 20km (4km) runs during the cold seasons (Fig. 5d). As shown later in section 4.3, both $NO_3$ and $NH_4$ simulations are quite sensitive to the PBL scheme applied.

OM, the second largest contributing species to cold season $PM_{2.5}$ in the SJV (Table 3), is significantly underestimated by 82% in the 20km simulation (Fig. 5f). The 4km simulation produces higher OM, but it is still lower than the IMPROVE observations by 63%. The underestimation of OM is expected, because SOA processes are not included in our model infrastructure. Fast et al. (2014) used the simplified two-product volatility basis set parameterization to simulate equilibrium SOA partitioning in WRF-Chem although SOA was still underestimated in their simulation. It remains ongoing research how to correctly represent SOA processes in regional climate models.

Both the 20km and 4km simulations reproduce the seasonal variability of EC, with a correlation of 0.98 between the modeled and observed time series (Table 2). The 20km simulation underestimates EC by 52% (16%) in the cold (warm) season (Fig. 5e and Table 3). The 4km simulated EC (1.12 μg $m^{-3}$) exhibits good agreement with IMPROVE (1.08 μg $m^{-3}$) in the cold season, but overestimates EC by 53% in the warm season.

The seasonal variability of $SO_4$ at Fresno is very different from other $PM_{2.5}$ species. It peaks in May at 1.35 μg $m^{-3}$ and reaches the minimum of 0.67 μg $m^{-3}$ in August (Fig. 5g). The 20km simulated $SO_4$ exhibits good correlation of 0.63 with the observation (Table 2), but is biased low

by 28% to 63% throughout WY2013 (Fig. 5g). Although the observed $SO_2$, the precursor of $SO_4$, has approximately similar seasonal variation to the observed $SO_4$ (Fig. 6b), the 20km simulated seasonal variability of $SO_2$ resembles other anthropogenic emissions, with high values in the cold season and low values in the warm season, out of phase with the simulated $SO_4$ and the observed $SO_2$. The 4km simulation produces higher $SO_4$ than the 20km run, resulting in better agreement with the observation (0.82 μg $m^{-3}$ vs. 0.87 μg $m^{-3}$) during the cold season (Fig. 5g and Table 3). However, the 4km run produces an increase of $SO_4$ by only 13% comparing to the 20km run in the warm season, resulting in a correlation of -0.16 between the 4km simulation and the observation.

To explore the possible cause for the underestimation of $SO_4$ and $SO_2$ in the warm season in both the 20km and 4km simulations, we conduct a sensitivity experiment with different chemical boundary conditions from the baseline runs (20km_BC1 in the supplementary). We find that $SO_4$ in the SJV is partly contributed to by marine intrusions (the different chemical boundary conditions between 20km_BC1 and 20km_D2) throughout the year (supplementary Fig. 2g), as pointed out by Fast et al. (2014). Including the marine intrusions, the 20km_BC1 simulated $SO_4$ tracks the observation at a correlation of 0.78. Doubled chemical boundary conditions in the 20km simulation results in 41% increase in $SO_4$ at Fresno, with a stronger increase in the warm season. Compared to the observed $SO_4$ of 1.04 μg $m^{-3}$ in the warm season, the simulated $SO_4$ of 0.79 μg $m^{-3}$ in the 20km_BC1 run is closer to the observation than that simulated in the 20km_D2 run (0.53 μg $m^{-3}$). The relative contributions of local emissions and remote transports (as well as other emission sources, such as wild fires) to $SO_4$ concentrations in different seasons of the SJV require further investigation.

Overall, the 4km simulation produces higher AOD and surface PM than the 20km simulation in urban areas of the SJV, especially during the cold season, resulting in better agreement with satellite and surface observations than the 20km simulation. Both the 20km and 4km simulations approximately capture the seasonal variability of $PM_{2.5}$ and most of its speciation. However, significant low biases of AOD and $PM_{10}$ are found during the warm season in both simulations. The underestimation also exists in a sensitivity experiment (not shown) with the same model setups except initialized in April, indicating that the identified model biases during the warm season are not caused by potential model drift after a relatively long simulation period. The relatively good performance in simulating $PM_{2.5}$ but not $PM_{10}$ during the warm season suggests that coarse aerosol particle mass (CM; 10 μm ≥ particulate matter with diameter > 2.5 μm), mainly dust in the SJV, is not properly represented in the model. The impact of dust parameterizations is investigated in the 4km_D2 experiment.

## 4.2 Sensitivity to Dust Scheme

Limited amounts of $PM_{2.5}$_dust (dust with diameter ≤ 2.5 μm) are observed in the SJV cold season, with a minimum of 0.37 μg $m^{-3}$ in December (Fig. 7a). The amount of $PM_{2.5}$_dust increases in the warm season, with a peak of 3.86 μg $m^{-3}$ in September. The 4km simulation produces comparable $PM_{2.5}$_dust relative to IMPROVE in the winter, but almost no dust in other months (Fig. 7 and upper panel in Fig. 8). On the other hand, the dust emission rate in the 4km_D2 run is significantly higher than the 4km run. We have found that the source function, *S*, for potential wind erosion in the SJV is set to zero in the 1° × 1° GOCART dataset used for the 4km simulation (Fig. 9). An updated source function, *S*, at higher resolution is needed for the GOCART dust scheme to correctly represent dust emissions in the SJV.

385 The 4km_D2 simulation reproduces the amount of $PM_{2.5}$_dust in OND (Fig. 7a). However,
386 it overestimates $PM_{2.5}$_dust by up to a factor of 3 in the warm season, resulting in an overestimation
387 of $PM_{2.5}$ by 52% (Fig. 7b and Table 3). $PM_{2.5}$_dust is not sensitive to long-range transport (from
388 chemical boundary conditions in the model simulation; Supplementary Fig. 2h). Both the 4km and
389 4km_D2 simulations capture the seasonal variability of $PM_{2.5}$, but not that of $PM_{10}$ (Fig. 7c). The
390 magnitude of $PM_{10}$ in the 4km_D2 run is larger than the 4km simulation. $PM_{10}$ in the 4km_D2 run
391 is overestimated in April-May-June (AMJ) but underestimated in July-August-September (JAS),
392 leading to a comparable season mean of 38.12 μg $m^{-3}$ with IMPROVE observed 34.82 μg $m^{-3}$. The
393 overestimation of AMJ $PM_{10}$ and $PM_{2.5}$_dust in the 4km_D2 run is likely associated with the high
394 bias in the simulated wind speed (Fig. 2b).

395 On the relative contribution of different aerosol species, IMPROVE observations at Fresno
396 show that $NO_3$ is the primary contributor (32.3%) to $PM_{2.5}$ while only 5.3% of $PM_{2.5}$ is dust in the
397 cold season (panel 1 of Fig. 10). Both the 4km and 4km_D2 runs roughly reproduce the relative
398 contributions to $PM_{2.5}$ in the cold season, with an overestimation of $NO_3$ and $NH_4$ and an
399 underestimation of OM, consistent with the time series in Fig. 5. Relative contributions of dust to
400 $PM_{2.5}$ are better simulated in the 4km_D2 run (7.3%) than the 4km one (<1.0%). IMPROVE shows
401 that 46.6% of $PM_{10}$ is CM in the cold season (panel 2 of Fig. 10). Both the 4km (6.3%) and
402 4km_D2 (20.6%) runs underestimate the contribution of CM to $PM_{10}$, mainly in October and
403 November. In the warm season, dust (24.6%) becomes the primary contributor to $PM_{2.5}$ while the
404 contribution from $NO_3$ decreases to 9.9% in IMPROVE observations (panel 3 of Fig. 10). Almost
405 no $PM_{2.5}$_dust is simulated in the 4km run while too much $PM_{2.5}$_dust is produced in the 4km_D2
406 (50.5%) run during the warm season. The relative contribution of CM to $PM_{10}$ is too small (27.6%)

in the 4km run, while the 4km_D2 run reflects an better relative contribution of 66.3% as compared to an IMPROVE observed 75.8% (panel 4 of Fig. 10).

AOD simulations are improved in the 4km_D2 experiment (Fig. 11), with better agreement found from MISR (Fig. 3) in AMJ. AOD (0.114) in the 4km_D2 run is comparable to observations (0.131) in AMJ, but still underestimated by 53% in JAS. Consistent with AOD, the vertical distribution of aerosol extinction is reasonably simulated during the cold season in the WRF-Chem simulations, while large discrepancies are found in the warm season (Fig. 12). As observed by CALIOP at 532 nm, aerosols are confined below 1 km in the cold season and decrease sharply with height. During AMJ, aerosols are well mixed between the surface and the altitude of 1.5 km and then decrease with height gradually. During JAS, the well-mixed aerosol layer is shallower than that in AMJ and the vertical profile of aerosol extinction is in-between the cold season and AMJ. Model simulations roughly capture the "bottom-heavy" structure of the extinction profiles observed by CALIOP especially in the cold season, but significant biases exist. One common problem for all four seasons is the low bias in the boundary layer and high bias in the free atmosphere. Similar discrepancy between the model simulations and CALIOP is shown in other studies (Wu et al., 2011a; Hu et al., 2016). The model does not capture the well-mixed aerosol layer during AMJ. The difference in the aerosol extinction profiles between the 4km and 4km_D2 runs is small during the cold season.

Dust in the boundary layer is a primary factor contributing to aerosol extinction in the SJV, as illustrated by the differences between the bulk seasonal CALIOP mean profile and those excluding the contributions of the dust and polluted dust (CALIOP_nodust) profiles (Fig. 12). Simulated aerosol extinction falls between the two in all seasons, suggesting that dust is the primary factor contributing to the model biases in aerosol extinction. Although a small portion of

430 $PM_{2.5}$ is dust in the cold season, it contributes to about 50% of total aerosol extinction (Fig. 12a
431 and 12b). A predominant portion of aerosol extinction in the lower troposphere is contributed by
432 dust in the warm season (Fig. 12c and 12d). There, the 4km_D2 simulation produces higher aerosol
433 extinction between 0.3 km and 3 km than the 4km simulation, although it is still lower than
434 CALIOP. The simulated aerosol extinction in the free troposphere is close to or larger than
435 CALIOP, suggesting that aerosols transported from remote areas through chemical boundary
436 conditions (e.g., the differences between the 20km_BC1 and 20km_D2 runs in Supplementary Fig.
437 3) may not be the major factor contributing to the underestimation of dust between 0.3 km and 3
438 km in the SJV.

439 Overall, the poor simulations of dust play a dominant role in the low bias of aerosols in the
440 boundary layer during the warm season. Both the GOCART and DUSTRAN dust emission
441 schemes used in this study have difficulties in reproducing dust emissions in the SJV, with an
442 underestimation in GOCART and an overestimation in DUSTRAN (Fig. 7). Improvement on the
443 dust emission schemes is needed for capturing the seasonal variability of aerosols in the SJV.

444 ## 4.3 The Role of Meteorology

445 The WRF-Chem simulations approximately reproduce the seasonal variations of
446 meteorological variables near the surface (correlations > 0.80), including temperature, RH, wind
447 speed and precipitation (Supplementary Fig. 6 and Supplementary Table 1). All of the model
448 simulations exhibit warm and dry biases near surface and in the boundary layer, with cold and wet
449 biases in the free atmosphere (Supplementary Fig. 6-8 and Supplementary Table 2). The dry bias
450 in the 4km_D2 run is about 10% near the surface throughout WY2013. Due to the relative dry
451 environment (RH<50%) in the warm season, the underestimation of boundary layer aerosol
452 extinction and column-integrated AOD is unlikely caused by the hygroscopic effects (Feingold

and Morley, 2003). In the cold season, the surface wind speed is underestimated by 0.67 m $s^{-1}$ (1.00 m $s^{-1}$) in the 4km_D2 (20km_D2) runs. In the warm season, the 4km_D2 run overestimates wind speed by 0.78 m $s^{-1}$, while the 20km_D2 run has an underestimation of 0.16 m $s^{-1}$. These results suggest that wind speed is not a major factor contributing to the low biases of aerosols in the boundary layer between 0.3 km and 3 km. Furthermore, the seasonal variability of precipitation is well captured in the simulations, while the magnitude of precipitation is weaker than the observations during the warm season (Supplementary Table 2). Thus, we conclude that wet removal processes would not be a primary reason for the aerosol biases in the warm season.

In the warm season, more aerosols are observed above 1.5 km than in the cold season (Fig. 12). A well-mixed layer of aerosols is observed below 1.5 km in AMJ (Fig. 12c), consistent with the unstable lower troposphere below 1.5 km shown in AIRS and ERA-Interim (Fig. 13c). The WRF-Chem model simulates neutral (or weakly stable) layers below 1.5 km, which may limit uplifting of aerosols from the surface, failing to create a deep well-mixed layer of aerosols (Fig. 12c). Although the dust emission at the surface is overestimated in AMJ in the 4km_D2 run, the simulated neutral or weakly stable thermal structure does not favor convective vertical mixing, resulting in the low biases of aerosols between 0.3 km and 3 km.

Similar biases of aerosol and instability in the lower troposphere are also shown in JAS (Fig. 12d and 13d). The stable boundary layer limits vertical transport of aerosols from the surface, contributing to the low bias of column-integrated AOD in JAS (Fig. 11). In JAS (Fig. 12d), aerosol extinction close to the CALIOP observation is simulated in the free atmosphere, suggesting that the low bias in AOD is not due to the halved chemical boundary conditions from MOZART-4. In the cold season, in spite of some discrepancies in the magnitude of atmospheric stability, all of the

475 simulations capture the stable lower troposphere (Fig. 13a and 13b), consistent with relatively
476 good performance of aerosol simulations in the cold season.

477 As biases in the model simulations are found mainly within the boundary layer, a sensitivity
478 experiment is conducted at 20 km resolution using the ACM2 PBL scheme (20km_P7). Although
479 the changes in the meteorological variables (Supplementary Fig. 6-9) and atmospheric static
480 stability (Fig. 13) are rather small, the simulated surface $NO_3$ and $NH_4$ in the 20km_P7 run
481 decrease by 50% compared to the 20km_D2 run (Fig. 14c, 14d and Table 3). Considering that
482 more $NO_3$ and $NH_4$ are simulated at 4 km resolution than at 20 km resolution as shown in section
483 4.1, the use of the ACM2 PBL scheme at 4 km simulation would largely resolve the high biases
484 of $NO_3$ and $NH_4$ in the 4km_D2 simulation. The decrease of $NO_3$ and $NH_4$ near the surface is
485 because more aerosols are transported to the layers above 0.5 km (Fig. 15a and 15b), possibly
486 resulting from different convective vertical mixing in the PBL schemes. However, $PM_{2.5}$_dust is
487 significantly overestimated by a factor of 4 in the 20km_P7 simulation (Fig. 14h), leading to a
488 small decrease of $PM_{2.5}$ by only 8% compared with the 20km_D2 run in the cold season. In the
489 warm season, $PM_{2.5}$_dust in the 20km_P7 run is overestimated by a factor of 5, causing an
490 overestimation of $PM_{2.5}$ and $PM_{10}$ (Fig. 14a and 14b). Aerosol extinctions in the boundary layer
491 above the surface increase in the warm season (Fig. 15c and 15d), possibly related to
492 overestimation of dust emissions and more conducive convective vertical transport in the PBL
493 scheme.

494 In summary, the WRF-Chem model captures the seasonal variations of meteorological
495 variables (temperature, RH, wind speed and precipitation), despite some deviations in magnitude.
496 The low biases in aerosol optical properties of the warm season likely do not originate from
497 hygroscopic effects, wet removal processes or dust emissions associated with the wind speed bias.

The model simulates a stable environment in the warm season, which is opposite to the observed unstable environment. The simulated stable environment may be most likely responsible for low biases in the aerosol extinction above the surface (0.3-3 km) and the column-integrated AOD in the warm season. Switching to the ACM2 PBL scheme leads to improved vertical displacement of aerosols in the boundary layer, thus an improvement in the simulations of $NO_3$ and $NH_4$ in the cold season. However, dust emissions are significantly overestimated with the ACM2 PBL scheme, which contributes partly to the better simulation of aerosol extinction in the boundary layer and AOD in the column. These results highlight that improving the simulation of boundary layer structure and processes are critical for capturing the vertical profiles of aerosol extinction.

## 4.4 Results in Rural Areas

In general, low values of PM concentration are observed in the rural areas, Pinnacles and Kaiser (Fig. 16 and 17). The rural areas share some similar model performance to the urban areas, such as the overestimation of $NO_3$, reasonable simulation of EC, good representation of $SO_4$ in the cold season and underestimation of $SO_4$ in the warm season. However, the results are not sensitive to model resolution. It suggests that high resolution is particularly important for heavily polluted areas due to the inhomogeneity of emission sources, but less important for relatively lightly polluted areas.

In late July/early August, MODIS (Moderate Resolution Imaging Spectroradiometer) fire data (not shown) showed active wild fires close to Kaiser, which resulted in high concentration of aerosols locally (Fig. 17). Our model simulations with monthly-varying fire emissions fail to reproduce these fire events. Previous studies (e.g., Grell et al., 2011; Wu et al. 2011a; Archer-Nicholls et al., 2015) demonstrated that the WRF-Chem model can capture aerosols distributions from wild fires based on fire locations from satellite observations. Campbell et al. (2016) further

described the difficulties in constraining total aerosol mass from operational satellite fire observations and the time needed by the model for diffusion within the near-surface layers to render both reasonable AOD and vertical profiles of aerosol extinction. For operational application of the WRF-Chem model in MAIA retrievals, the observations of daily fire events need to be more appropriately considered.

## 5. Summary

The WRF-Chem (Weather Research and Forecasting model with Chemistry) model is employed to simulate the seasonal variability of aerosols in WY2013 (water year 2013) in the SJV (San Joaquin Valley). Model simulations are evaluated using satellite and in-situ observations. In general, the model simulations conducted at 4 km resolution reproduce the spatial and temporal variations of regional aerosols in the cold season, when aerosols are mainly contributed to by anthropogenic emissions in the SJV. The magnitude of simulated aerosols in the cold season however, especially in relatively dense urban areas, is sensitive to model horizontal resolution. The 4km simulation has comparable magnitude to available observations, while the 20km simulation underestimates aerosols. Differences in aerosol simulation fidelity as a function of variable resolutions are mainly due to the difference in aerosol emissions and simulated precipitation. Emissions at higher resolution can better resolve the inhomogeneity of anthropogenic emissions in the SJV than at lower resolution. The sensitivity to horizontal resolution is small in rural areas and during warm season, where/when the relative contribution of anthropogenic emissions is small.

Previous studies in the SJV are mainly focused on $PM_{2.5}$ (particulate matter with diameter $\leq 2.5$ μm) and during cold season (e.g. Chow et al., 2006; Herner et al., 2006; Pun et al., 2009; Ying and Kleeman, 2009; Zhang et al., 2010; Chen et al., 2014; Hasheminassab et al., 2014; Kelly

et al., 2014; Baker et al., 2015; Brown et al., 2016). CALIOP (Cloud-Aerosol Lidar with Orthogonal Polarization) and IMPROVE (Interagency Monitoring of Protected Visual Environments) observations show that dust is a primary contributor to the aerosols in the SJV, especially in the warm season. Dust contributes 24.6% to $PM_{2.5}$ while more than 75.8% to $PM_{10}$ in the warm season. For all seasons, the major component of aerosol extinction in the boundary layer is dust as observed by CALIOP, consistent with Kassianov et al. (2012). For a complete understanding of aerosol impacts on air quality, weather and climate, the full spectrum of aerosols should be considered during all seasons.

All the model simulations conducted fail to capture aerosol vertical distribution and variability in the SJV warm season, largely due to the misrepresentation of dust emissions, static stability and vertical mixing in the boundary layer. The GOCART (Goddard Global Ozone Chemistry Aerosol Radiation and Transport) dust emission scheme significantly underestimates dust due to the non-active source function, *S*, for potential wind erosion used in this study while the DUSTRAN (DUST TRANsport model) scheme may overestimate dust emission in the SJV. Along with the bias in dust emissions, our simulations produce a relatively stable boundary layer in the warm season, in contrast with observations suggesting a more unstable environment, leading to a weak vertical mixing of aerosols in the boundary layer. Improved dust emission and better simulations of the boundary layer properties are needed for accurate simulation of aerosols in the SJV warm season.

Other biases are also identified in the model simulations. $NO_3$ and $NH_4$ in the cold season are overestimated in the model, but the results are sensitive to the choice of the PBL (planetary boundary layer) scheme. The SOA (secondary organic aerosol) processes contribute to the underestimation of OM (organic matter) in this study. The underestimation of sulfate in the warm

567 season may be caused by the misrepresentation of emissions and the chemical boundary conditions
568 related to marine intrusions. Aerosols from wild fires are not captured in the simulations with
569 monthly updated fire data. Further investigations are needed to improve model simulations in the
570 SJV for both scientific and operational applications.

## 571 Acknowledgements

572 This study was carried out at the Jet Propulsion Laboratory, California Institute of
573 Technology, under a contract with the National Aeronautics and Space Administration. The
574 authors thank the funding support from the NASA ACMAP program and JPL PDF program. This
575 work is partially sponsored by California Energy Commission under grant #EPC-14-064. Author
576 JRC acknowledges the support of the NASA ACCDAM program and its manager Hal Maring.
577 The authors thank the three anonymous reviewers for their helpful comments.

## 578 References

579 Archer-Nicholls, S., Lowe, D., Darbyshire, E., Morgan, W. T., Bela, M. M., Pereira, G., Trembath,
580 J., Kaiser, J. W., Longo, K. M., Freitas, S. R., Coe, H., and McFiggans, G.: Characterising
581 Brazilian biomass burning emissions using WRF-Chem with MOSAIC sectional aerosol,
582 Geosci. Model Dev., 8, 549-577, doi:10.5194/gmd-8-549-2015, 2015.

583 Ångström, A.: On the atmospheric transmission of Sun radiation and on dust in the air, Geogr.
584 Ann., 11, 156–166, 1929.

585 Baker, K. R., Carlton, A. G., Kleindienst, T. E., Offenberg, J. H., Beaver, M. R., Gentner, D. R.,
586 Goldstein, A. H., Hayes, P. L., Jimenez, J. L., Gilman, J. B., de Gouw, J. A., Woody, M. C.,
587 Pye, H. O. T., Kelly, J. T., Lewandowski, M., Jaoui, M., Stevens, P. S., Brune, W. H., Lin, Y.-
588 H., Rubitschun, C. L., and Surratt, J. D.: Gas and aerosol carbon in California: comparison of
589 measurements and model predictions in Pasadena and Bakersfield, Atmos. Chem. Phys., 15,
590 5243-5258, doi:10.5194/acp-15-5243-2015, 2015.

591 Banks, R.F., Baldasano, J.M.: Impact of WRF model PBL schemes on air quality simulations over
592 Catalonia, Spain. Science of the Total Environment, 572, 98-113,
593 http://dx.doi.org/10.1016/j.scitotenv.2016.07.167, 2016.

594 Banks, R. F., Tiana-Alsina, J., Baldasano, J. M., Rocadenbosch, F., Papayannis, A., Solomos, S.,
595 and Tzanis, C. G.: Sensitivity of boundary-layer variables to PBL schemes in the WRF model
596 based on surface meteorological observations, lidar, and radiosondes during the HygrA-CD
597 campaign, Atmos. Res., 176, 185–201, 2016.

598 Barnard, J. C., Fast, J. D., Paredes-Miranda, G., Arnott, W. P., and Laskin, A.: Technical Note:
599 Evaluation of the WRF-Chem "Aerosol Chemical to Aerosol Optical Properties" Module using
600 data from the MILAGRO campaign, Atmos. Chem. Phys., 10, 7325–7340, doi:10.5194/acp-
601 10-7325-2010, 2010.

602 Brown, S. G., Hyslop, N. P., Roberts, P. T., McCarthy, M. C., and Lurmann, F. W.: Wintertime
603 vertical variations in particulate matter (PM) and precursor concentrations in the San Joaquin
604 Valley during the California Regional Coarse PM/Fine PM Air Quality Study, J. Air Waste
605 Manage., 56, 1267–1277, 2006.

606 Campbell, J. R., Tackett, J. L., Reid, J. S., Zhang, J., Curtis, C. A., Hyer, E. J., Sessions, W. R.,
607 Westphal, D. L., Prospero, J. M., Welton, E. J., Omar, A. H., Vaughan, M. A., and Winker, D.
608 M.: Evaluating nighttime CALIOP 0.532 μm aerosol optical depth and extinction coefficient
609 retrievals, Atmos. Meas. Tech., 5, 2143-2160, doi:10.5194/amtd-5-2143-2012, 2012.

610 Campbell., J. R., Ge, C., Wang, J., Welton, E. J., Bucholtz, A., Hyer, E. J., Reid, E. A., Chew, B.
611 N., Liew, S.-C., Salinas, S. V., Lolli, S., Kaku, K. C., Lynch, P., Mahmud, M., Mohamad, M.,
612 and Holben, B. N.: Applying Advanced Ground-Based Remote Sensing in the Southeast Asian
613 Maritime Continent to Characterize Regional Proficiencies in Smoke Transport Modeling, J.
614 Appl. Meteorol. Climatol., 55, 3-22, doi: http://dx.doi.org/10.1175/JAMC-D-15-0083.1, 2016.

615 Chapman, E. G., Gustafson Jr., W. I., Easter, R. C., Barnard, J. C., Ghan, S. J., Pekour, M. S., and
616 Fast, J. D.: Coupling aerosolcloud-radiative processes in the WRF-Chem model: Investigating
617 the radiative impact of elevated point sources, Atmos. Chem. Phys., 9, 945–964,
618 doi:10.5194/acp-9-945-2009, 2009.

Chen, D., Xie, X., Zhou, Y., Lang, J., Xu, T., Yang, N., Zhao, Y., and Liu, X.: Performance Evaluation of the WRF-Chem Model with Different Physical Parameterization Schemes during an Extremely High PM2.5 Pollution Episode in Beijing. Aerosol and Air Quality Research, 17:262-277. doi: 10.4209/aaqr.2015.10.0610, 2017.

Chen, J., Lu, J., Avise, J. C., DaMassa, J. A., Kleeman, M. J., and Kaduwela, A. P.: Seasonal modeling of PM2.5 in California's San Joaquin Valley, Atmos. Environ., 92, 182–190, 2014.

Chew, B. N., J. R. Campbell, J. S. Reid, D. M. Giles, E. J. Welton, S. V. Salinas and S. C. Liew: Tropical cirrus cloud contamination in sun photometer data, Atmos. Env., 45, 6724-6731, doi:10.1016/j.atmosenv.2011.08.017, 2011.

Chow, J. C., Chen, L. W. A., Watson, J. G., Lowenthal, D. H., Magliano, K. A., Turkiewicz, K., Lehrman, D. E.: PM2.5 chemical composition and spatiotemporal variability during the California regional PM10/PM2.5 air quality study (CRPAQS), J. Geophys. Res.-Atmos., 111, D10S04, doi:10.1029/2005JD006457, 2006.

Cuchiara, G.C., Li, X., Carvalho, J., and Rappenglück, B.: Intercomparison of planetary boundary layer parameterization and its impacts on surface ozone concentration in the WRF/Chem model for a case study in Houston/Texas. Atmospheric Environment, 96,175–185. http://dx.doi.org/10.1016/j.atmosenv.2014.07.013, 2014.

Dee, D. P., Uppala, S. M., Simmons, A. J., Berrisford, P., Poli, P, Kobayashi, S., Andrae, U., Balmaseda, M. A., Balsamo, G., Bauer, P., Bechtold, P., Beljaars, A. C. M., van de Berg, L., Bidlot, J., Bormann, N., Delsol, C., Dragani, R., Fuentes, M., Geer, A. J., Haimberger, L., Healy, S. B., Hersbach, H., Hólm, E. V., Isaksen, L., Kallberg, P., Köhler, M., Matricardi, M., McNally, A. P., Monge-Sanz, B. M., Morcrette, J.-J., Park, B.-K., Peubey, C., de Rosnay, P., Tavolato, C., Thépaut, J.-N., and Vitart, F.: The ERA-Interim reanalysis: configuration and performance of the data assimilation system, Q. J. R. Meteorol. Soc., 137, 553–597, 2011.

Diner, D. J., Beckert, J. C., Reilly, T. H., Bruegge, C. J., Conel, J. E., Kahn, R. A., Martonchik, J. V., Ackerman, T. P., Davies, R., Gerstl, S. A. W., Gordon, H. R., Muller, J. P., Myneni, R. B., Sellers, P. J., Pinty, B., and Verstraete, M. M.: Multi-angle Imaging SpectroRadiometer (MISR) Instrument Description and Experiment Overview, IEEE T. Geosci. Remote, 36, 1072–1087, 1998.

Divakarla, M. G., Barnet, C. D., Goldberg, M. D., McMillin, L. M., Maddy, E., Wolf, W., Zhou, L., and Liu, X.: Validation of Atmospheric Infrared Sounder temperature and water vapor retrievals with matched radiosonde measurements and forecasts, J. Geophys. Res., 111, D09S15, doi:10.1029/2005JD006116, 2006.

Eck, T. F., Holben, B. N., Reid, J. S., Dubovik, O., Smirnov, A., O'Neill, N. T., Slutsker, I., and Kinn, S.: Wavelength dependence of the optical depth of biomass burning urban, and desert dust aerosols, J. Geophys. Res., 104, 31333–31349, 1999.

Emmons, L. K., Walters, S., Hess, P. G., Lamarque, J.-F., Pfister, G. G., Fillmore, D., Granier, C., Guenther, A., Kinnison, D., Laepple, T., Orlando, J., Tie, X., Tyndall, G., Wiedinmyer, C., Baughcum, S. L., and Kloster, S.: Description and evaluation of the Model for Ozone and Related chemical Tracers, version 4 (MOZART-4), Geosci. Model Dev., 3, 43–67, doi: 10.5194/gmd-3-43-2010, 2010.

Fast, J. D., Gustafson Jr., W. I., Easter, R. C., Zaveri, R. A., Barnard, J. C., Chapman, E. G., Grell, G. A. and Peckham, S. E.: Evolution of ozone, particulates, and aerosol direct radiative forcing in the vicinity of Houston using a fully coupled meteorology-chemistry-aerosol model, J. Geophys. Res., 111, D21305, doi:10.1029/2005JD006721, 2006.

Fast, J. D., Gustafson Jr., W. I., Berg, L. K., Shaw, W. J., Pekour, M., Shrivastava, M., Barnard, J. C., Ferrare, R. A., Hostetler, C. A., Hair, J. A., Erickson, M., Jobson, B. T., Flowers, B., Dubey, M. K., Springston, S., Pierce, R. B., Dolislager, L., Pederson, J., and Zaveri, R. A.: Transport and mixing patterns over Central California during the carbonaceous aerosol and radiative effects study (CARES), Atmos. Chem. Phys., 12, 1759-1783, doi:10.5194/acp-12-1759-2012, 2012.

Fast, J. D., Allan, J., Bahreini, R., Craven, J., Emmons, L., Ferrare, R., Hayes, P. L., Hodzic, A., Holloway, J., Hostetler, C., Jimenez, J. L., Jonsson, H., Liu, S., Liu, Y., Metcalf, A., Middlebrook, A., Nowak, J., Pekour, M., Perring, A., Russell, L., Sedlacek, A., Seinfeld, J., Setyan, A., Shilling, J., Shrivastava, M., Springston, S., Song, C., Subramanian, R., Taylor, J. W., Vinoj, V., Yang, Q., Zaveri, R. A., and Zhang, Q.: Modeling regional aerosol and aerosol precursor variability over California and its sensitivity to emissions and long-range transport during the 2010 CalNex and CARES campaigns, Atmos. Chem. Phys., 14, 10013-10060, doi:10.5194/acp-14-10013-2014, 2014.

678 Feingold, G., and Morley, B.: Aerosol hygroscopic properties as measured by lidar and comparison
679 with in situ measurements, J. Geophys. Res., 108(D11), 4327, doi:10.1029/2002JD002842,
680 2003.

681 Flanner, M. G., and Zender, C. S.: Snowpack radiative heating: Influence on Tibetan Plateau
682 climate, Geophys. Res. Lett., 32, L06501, doi:10.1029/2004GL022076, 2005.

683 Flanner, M. G., and Zender, C. S.: Linking snowpack microphysics and albedo evolution, J.
684 Geophys. Res., 111, D12208, doi:10.1029/2005JD006834, 2006.

685 Fountoukis, C., Koraj, D., Denier van der Gon, H. A. C., Charalampidis, P. E., Pilinis, C., and
686 Pandis, S. N.: Impact of grid resolution on the predicted fine PM by a regional 3-D chemical
687 transport model, Atmos. Environ., 68, 24–32, 2013.

688 Freitas, S. R., Longo, K. M., Alonso, M. F., Pirre, M., Marecal, V., Grell, G., Stockler, R., Mello,
689 R. F., and Sánchez Gácita, M.: PREP-CHEM-SRC – 1.0: a preprocessor of trace gas and
690 aerosol emission fields for regional and global atmospheric chemistry models, Geosci. Model
691 Dev., 4, 419-433, doi:10.5194/gmd-4-419-2011, 2011.

692 Gao, Y., Liu, X., Zhao, C., and Zhang, M.: Emission controls versus meteorological conditions in
693 determining aerosol concentrations in Beijing during the 2008 Olympic Games, Atmos. Chem.
694 Phys., 11, 12437-12451, doi:10.5194/acp-11-12437-2011, 2011.

695 Ghan, S., Laulainen, N., Easter, R., Wagener, R., Nemesure, S., Chapman, E., Zhang, Y., and
696 Leung, R.: Evaluation of aerosol direct radiative forcing in MIRAGE, J. Geophys. Res.,
697 106(D6), 5295–5316, doi:10.1029/2000JD900502, 2001.

698 Ginoux, P., Chin, M., Tegen, I., Prospero, J. M., Holben, B., Dubovik, O., and Lin, S.: Sources
699 and distributions of dust aerosols simulated with the GOCART model, J. Geophys. Res., 106,
700 20225–20273, 2001.

701 Gong, S. L.: A parameterization of sea-salt aerosol source function for sub- and super-micron
702 particles, Global Biogeochem. Cy., 17, 1097, doi:10.1029/2003GB002079, 2003.

703 Grell, G. and Devenyi, D.: A generalized approach to parameterizing convection combining
704 ensemble and data assimilation techniques, Geophys. Res. Lett., 29(14),
705 doi:10.1029/2002GL015311, 2002.

706 Grell, G., Peckham, S., Schmitz, R., et al.: Fully coupled "online" chemistry within the WRF
707 model, Atmos. Environ., 39(37), 6957–6975, 2005.

708 Grell, G., Freitas, S. R., Stuefer, M., and Fast, J.: Inclusion of biomass burning in WRF-Chem:
709 impact of wildfires on weather forecasts, Atmos. Chem. Phys., 11, 5289-5303,
710 doi:10.5194/acp-11-5289-2011, 2011.

711 Guenther, A., Karl, T., Harley, P., Wiedinmyer, C., Palmer, P. I., and Geron, C.: Estimates of
712 global terrestrial isoprene emissions using MEGAN (Model of Emissions of Gases and
713 Aerosols from Nature), Atmos. Chem. Phys., 6, 3181–3210, doi: 10.5194/acp-6-3181-2006,
714 2006.

715 Hand, J., Copeland, S. A., Day, D. E., Dillner, A. M., Indresand, H., Malm, W. C., McDade, C.
716 E., Moore Jr., C. T., Pitchford, M. L., Schichtel, B. A., and Watson, J. G.: Spatial and seasonal
717 patterns and temporal variability of haze and its constituents in the United States: Report V,
718 June 2011, available at: http://vista.cira.colostate.edu/Improve/spatial-and-seasonal-patterns-
719 and-temporal-variability-of-haze-and-its-constituents-in-the-united-states-report-v-june-
720 2011/, 2011.

721 Hasheminassab, S., Daher, N., Saffari, A., Wang, D., Ostro, B. D., and Sioutas, C.: Spatial and
722 temporal variability of sources of ambient fine particulate matter ($PM_{2.5}$) in California, Atmos.
723 Chem. Phys., 14, 12085-12097, doi:10.5194/acp-14-12085-2014, 2014.

724 Herner, J. D., Ying, Q., Aw, J., Gao, O., Chang, D. P. Y., and Kleeman, M.: Dominant mechanisms
725 that shape the airborne particle size and composition in central California, Aerosol Sci.
726 Technol., 40, 827–844, 2006.

727 Holben, B. N., Eck, T. F., Slutsker, I., Tanre ì, D., Buis, J. P., Setzer, A., Vermote, E., Reagan, J.
728 A., Kaufman, Y. J., Nakajima, T., Lavenu, F., Jankowiak, I., and Smirnov, A.: AERONET –
729 A Federated Instrument Network and Data Archive for Aerosol Characterization, Remote
730 Sens. Environ., 66, 1–16, 1998.

731 Holben, B. N., Tanr, D., Smirnov, A., Eck, T. F., Slutsker, I., Abuhassan, N., Newcomb, W. W.,
732 Schafer, J. S., Chatenet, B., Lavenu, F., Kaufman, Y. J., Castle, J. V., Setzer, A., Markham,
733 B., Clark, D., Frouin, R., Halthore, R., Karneli, A., O'Neill, N. T., Pietras, C., Pinker, R. T.,

734 Voss, K., and Zibordi, G.: An emerging ground-based aerosol climatology: Aerosol optical
735 depth from AERONET, J. Geophys. Res., 106, 12067–12097, 2001.

736 Hong, S., Noh, Y., and Dudhia, J.: A new vertical diffusion package with an explicit treatment of
737 entrainment processes, Mon. Weather Rev., 134, 2318–2341, 2006.

738 Hu, X. M., Nielsen-Gammon, J.W., and Zhang, F.: Evaluation of three planetary boundary layer
739 schemes in the WRF model, J. Appl. Meteorol. Climatol., 49(9), 1831–1844,
740 doi:10.1175/2010JAMC2432.1, 2010.

741 Hu, Z., Zhao, C., Huang, J., Leung, L. R., Qian, Y., Yu, H., Huang, L., and Kalashnikova, O. V.:
742 Trans-Pacific transport and evolution of aerosols: evaluation of quasi-global WRF-Chem
743 simulation with multiple observations, Geosci. Model Dev., 9, 1725-1746, doi:10.5194/gmd-
744 9-1725-2016, 2016.

745 Iacono, M. J., Delamere, J. S., Mlawer, E. J., Shephard, M. W., Clough, S. A., and Collins, W. D.:
746 Radiative forcing by long-lived greenhouse gases: calculations with the AER radiative transfer
747 models, J. Geophys. Res., 113, D13103, doi:10.1029/2008JD009944, 2008.

748 Jaeglé, L., Quinn, P. K., Bates, T. S., Alexander, B., and Lin, J.-T.: Global distribution of sea salt
749 aerosols: new constraints from in situ and remote sensing observations, Atmos. Chem. Phys.,
750 11, 3137–3157, doi:10.5194/acp-11-3137-2011, 2011.

751 Kahn, R. A., Gaitley, B. J., Garay, M. J., Diner, D. J., Eck, T. F., Smirnov, A., and Holben, B. N.:
752 Multiangle Imaging SpectroRadiometer global aerosol product assessment by comparison with
753 the Aerosol Robotic Network, J. Geophys. Res., 115, D23209, doi:10.1029/2010JD014601,
754 2010.

755 Kassianov, E., Pekour, M., and Barnard, J.: Aerosols in central California: Unexpectedly large
756 contribution of coarse mode to aerosol radiative forcing, Geophys. Res. Lett., 39, L20806, doi:
757 10.1029/2012GL053469, 2012.

758 Kelly, J. T., Baker, K. R., Nowak, J. B., Murphy, J. G., Markovic, M. Z., VandenBoer, T. C., Ellis,
759 R. A., Neuman, J. A., Weber, R. J., and Roberts, J. M.: Fine-scale simulation of ammonium
760 and nitrate over the South Coast Air Basin and San Joaquin Valley of California during
761 CalNex-2010, J. Geophys. Res.-Atmos., 119, 3600–3614, 2014.

762 Lawrence, D. M., Oleson, K. W., Flanner, M. G., Thornton, P. E., Swenson, S. C., Lawrence, P.
763 J., Zeng, X., Yang, Z.-L., Levis, S., Sakaguchi, K., Bonan, G. B., and Slater, A. G.:
764 Parameterization improvements and functional and structural advances in version 4 of the
765 Community Land Model, J. Adv. Model. Earth Sys., 3, M03001, doi:
766 10.1029/2011MS000045, 2011.

767 Misenis, C. and Zhang, Y.: An examination of sensitivity of WRF/Chem predictions to physical
768 parameterizations, horizontal grid spacing, and nesting options, Atmos. Res., 97, 315–334,
769 doi:10.1016/j.atmosres.2010.04.005, 2010.

770 Morabito, D., Wu, L., and Slobin, S.: Weather Forecasting for Ka-band Operations: Initial Study
771 Results, IPN PR 42-206, pp. 1-24, August 15, 2016. Available at:
772 http://ipnpr.jpl.nasa.gov/progress_report/42-206/206C.pdf, 2016.

773 Morrison, H., Thompson, G., and Tatarskii, V.: Impact of cloud microphysics on the development
774 of trailing stratiform precipitation in a simulated squall line: comparison of one- and two-
775 moment schemes, Mon. Weather Rev., 137, 991–1007, 2009.

776 Omar, A.H., Winker, D.M., Kittaka, C., Vaughan, M.A., Liu, Z., Hu, Y., Trepte, C.R., Rogers,
777 R.R., Ferrare, R.A., Lee, K.P., Kuehn, R.E., Hostetler, C.A.: The CALIPSO automated aerosol
778 classification and lidar ratio selection algorithm. J. Atmos. Ocean. Technol. 26, 1994–2014,
779 2009.

780 Pleim, J. E.: A combined local and nonlocal closure model for the atmospheric boundary layer.
781 Part I: Model description and testing, J. Appl. Meteorol. Clim., 46, 1383–1395, 2007.

782 Pun, B. K., Balmori, R. T. F., and Seigneur, C.: Modeling wintertime particulate matter formation
783 in central California, Atmos. Environ., 43, 402–409, 2009.

784 Qian, Y., Gustafson Jr., W. I., and Fast, J. D.: An investigation of the sub-grid variability of trace
785 gases and aerosols for global climate modeling, Atmos. Chem. Phys., 10, 6917-6946,
786 doi:10.5194/acp-10-6917-2010, 2010.

787 Randerson, J. T., van der Werf, G. R., Giglio, L., Collatz, G. J., and Kasibhatla, P. S.: Global Fire
788 Emissions Database, Version 2 (GFEDv2.1). Data set. Available on-line [http://daac.ornl.gov/]
789 from Oak Ridge National Laboratory Distributed Active Archive Center, Oak Ridge,
790 Tennessee, U.S.A. doi:10.3334/ORNLDAAC/849, 2007.

San Joaquin Valley Air Pollution Control District: 2012 PM2.5 plan. Available from: http://www.valleyair.org/Air_Quality_Plans/PM25Plans2012.htm, 2012.

Scarino, A. J., Obland, M. D., Fast, J. D., Burton, S. P., Ferrare, R. A., Hostetler, C. A., Berg, L. K., Lefer, B., Haman, C., Hair, J. W., Rogers, R. R., Butler, C., Cook, A. L., and Harper, D. B.: Comparison of mixed layer heights from airborne high spectral resolution lidar, ground-based measurements, and the WRF-Chem model during CalNex and CARES, Atmos. Chem. Phys., 14, 5547-5560, doi:10.5194/acp-14-5547-2014, 2014.

Shaw, W., Allwine, K. J., Fritz, B. G., Rutz, F. C., Rishel, J. P., and Chapman, E. G.: An evaluation of the wind erosion module in DUSTRAN, Atmos. Environ., 42, 1907–1921, 2008.

Solomon, P. A., Crumpler, D., Flanagan, J. B., Jayanty, R. K. M., Rickman, E. E., and McDade C. E.: U.S. National PM 2.5 Chemical Speciation Monitoring Networks – CSN and IMPROVE: Description of Networks, J. Air Waste Manage., 64, 1410–1438, doi:10.1080/10962247.2014.956904, 2014.

Susskind, J., Barnet, C. D., and Blaisdell, J.: Retrieval of atmospheric and surface parameters from AIRS/AMSU/HSB data under cloudy conditions, IEEE Trans. Geosci. Remote Sens., 41(2), 390–409, doi:10.1109/TGRS.2002.808236, 2003.

Schuster, G. L., Dubovik, O., and Holben, B. N.: Angström exponent and bimodal aerosol size distributions, J. Geophys. Res., 111, D07207, doi:10.1029/2005JD006328, 2006.

Tessum, C. W., Hill, J. D., and Marshall, J. D.: Twelve-month, 12 km resolution North American WRF-Chem v3.4 air quality simulation: performance evaluation, Geosci. Model Dev., 8, 957-973, doi:10.5194/gmd-8-957-2015, 2015.

Toth, T. D., Campbell, J. R., Reid, J. S., Tackett, J. L., Vaughan, M. A. and Zhang, J.: Lower daytime threshold sensitivities to aerosol optical thickness in CALIPSO Level 2 products, J. Geophys. Res., in review, 2017.

US Environmental Protection Agency, 2010: Technical Support Document: Preparation of Emissions Inventories for the Version 4, 2005-based Platform, 73 pp., Office of Air Quality Planning and Standards, Air Quality Assessment Division, available at: https://www3.epa.gov/crossstaterule/pdfs/2005_emissions_tsd_07jul2010.pdf, 2010.

819 Wu, L., and Petty, G. W. : Intercomparison of Bulk Microphysics Schemes in Simulations of Polar
820 lows. Mon. Wea. Rev., 138, 2211-2228. doi: 10.1175/2010MWR3122.1, 2010.

821 Wu, L., Su, H. and Jiang, J. H.: Regional simulations of deep convection and biomass burning
822 over South America: 1. Model evaluations using multiple satellite data sets, J. Geophys. Res.,
823 116, D17208, doi:10.1029/2011JD016105, 2011a.

824 Wu, L., Su, H. and Jiang, J. H.: Regional simulations of deep convection and biomass burning
825 over South America: 2. Biomass burning aerosol effects on clouds and precipitation, J.
826 Geophys. Res., 116, D17209, doi:10.1029/2011JD016106, 2011b.

827 Wu, L., Su, H. and Jiang, J. H.: Regional simulations of aerosol impacts on precipitation during
828 the East Asian summer monsoon. J. Geophys. Res. Atmos., 118, doi: 10.1002/jgrd.50527,
829 2013.

830 Wu, L., Li, J.-L. F., Pi, C.-J., Yu, J.-Y., and Chen, J.-P.: An observationally based evaluation of
831 WRF seasonal simulations over the Central and Eastern Pacific, J. Geophys. Res. Atmos., 120,
832 doi:10.1002/2015JD023561, 2015.

833 Xie, B., Fung, J. C. H., Chan, A., and Lau, A.: Evaluation of nonlocal and local planetary boundary
834 layer schemes in the WRF model, J. Geophys. Res., 117, D12103, doi:10.1029/2011JD017080,
835 2012.

836 Ying, Q. and Kleeman, M. J.: Regional contributions to airborne particulate matter in central
837 California during a severe pollution episode, Atmos. Environ., 43, 1218–1228, 2009.

838 Young, S.A. and Vaughan, M.A.: The retrieval of profiles of particulate extinction from Cloud–
839 Aerosol Lidar Infrared Pathfinder Satellite Observations (CALIPSO) data: algorithm
840 description. J. Atmos. Ocean. Technol. 26, 1105–1119, 2009.

841 Zaveri, R. A. and Peters, L. K.: A new lumped structure photochemical mechanism for large-scale
842 applications, J. Geophys. Res., 104, 30387–30415, 1999.

843 Zaveri, R. A., Easter, R. C., Fast, J. D., and Peters, L. K.: Model for Simulating Aerosol
844 Interactions and Chemistry (MOSAIC), J. Geophys. Res., 113, D13204,
845 doi:10.1029/2007JD008782, 2008.

846 Zhang, Y., Liu, P., Liu, X.-H., Pun, B., Seigneur, C., Jacobson, M. Z., and Wang, W.-X.: Fine
847 scale modeling of wintertime aerosol mass, number, and size distributions in central California,
848 J. Geophys. Res.-Atmos., 115, D15207, doi:10.1029/2009jd012950, 2010.

849 Zhao, C., Liu, X., Leung, L. R., Johnson, B., McFarlane, S. A., Gustafson Jr., W. I., Fast, J. D.,
850 and Easter, R.: The spatial distribution of mineral dust and its shortwave radiative forcing over
851 North Africa: modeling sensitivities to dust emissions and aerosol size treatments, Atmos.
852 Chem. Phys., 10, 8821–8838, doi: 10.5194/acp-10-8821-2010, 2010.

853 Zhao, C., Liu, X., Ruby Leung, L., and Hagos, S.: Radiative impact of mineral dust on monsoon
854 precipitation variability over West Africa, Atmos. Chem. Phys., 11, 1879–1893,
855 doi:10.5194/acp-11-1879-2011, 2011.

856 Zhao, C., Chen, S., Leung, L. R., Qian, Y., Kok, J. F., Zaveri, R. A., and Huang, J.: Uncertainty in
857 modeling dust mass balance and radiative forcing from size parameterization, Atmos. Chem.
858 Phys., 13, 10733-10753, doi:10.5194/acp-13-10733-2013, 2013a.

859 Zhao, C., Leung, L. R., Easter, R., Hand, J., and Avise, J.: Characterization of speciated aerosol
860 direct radiative forcing over California, J. Geophys. Res., 118, 2372–2388, doi:
861 10.1029/2012JD018364, 2013b.

862 Zhao, C., Hu, Z., Qian, Y., Ruby Leung, L., Huang, J., Huang, M., Jin, J., Flanner, M. G., Zhang,
863 R., Wang, H., Yan, H., Lu, Z., and Streets, D. G.: Simulating black carbon and dust and their
864 radiative forcing in seasonal snow: a case study over North China with field campaign
865 measurements, Atmos. Chem. Phys., 14, 11475-11491, doi:10.5194/acp-14-11475-2014,
866 2014.

867 # List of Table

868 Table 1. Experiment description

| Experiment ID | Experiment description |
|---|---|
| 20km | Simulation with the GOCART dust scheme at 20 km horizontal resolution. |
| 20km_D2 | Same as 20km, but with the DUSTRAN dust scheme. |
| 20km_P7 | Same as 20km_D2, but with the ACM2 PBL scheme. |
| 4km | Same as 20km, but at 4 km horizontal resolution. |
| 4km_D2 | Same as 4km, but with the DUSTRAN dust scheme. |

869

870 Table 2. Correlation with observations for different species at Fresno, CA

| Species | 20km | 4km | 4km_D2 | 20km_D2 | 20km_P7 |
|---|---|---|---|---|---|
| $PM_{2.5}$ | 0.89 | 0.90 | 0.86 | 0.78 | 0.03 |
| $PM_{2.5}\_NO_3$ | 0.94 | 0.95 | 0.94 | 0.94 | 0.91 |
| $PM_{2.5}\_NH_4$ | 0.97 | 0.96 | 0.96 | 0.98 | 0.96 |
| $PM_{2.5}$_OM | 0.93 | 0.93 | 0.94 | 0.93 | 0.91 |
| $PM_{2.5}$_EC | 0.98 | 0.98 | 0.98 | 0.98 | 0.96 |
| $PM_{2.5}\_SO_4$ | 0.63 | -0.16 | -0.14 | 0.61 | 0.63 |
| $PM_{2.5}$_dust | -0.55 | -0.50 | 0.48 | 0.55 | 0.36 |
| $PM_{10}$ | -0.25 | -0.23 | -0.08 | 0.01 | -0.03 |

871

872 Table 3. Surface aerosol mass (μg $m^{-3}$) for different species at Fresno, CA

| Species | Cold season | | | | | | Warm season | | | | | |
|---|---|---|---|---|---|---|---|---|---|---|---|---|
| | OBS | 20km | 4km | 4km_D2 | 20km_D2 | 20km_P7 | OBS | 20km | 4km | 4km_D2 | 20km_D2 | 20km_P7 |
| $PM_{2.5}$ | 16.84 | 13.71 | 21.38 | 22.48 | 14.90 | 13.77 | 8.44 | 4.91 | 6.29 | 12.85 | 10.12 | 14.85 |
| $PM_{2.5}$_$NO_3$ | 5.43 | 6.36 | 9.54 | 9.22 | 6.22 | 3.16 | 0.84 | 0.55 | 0.69 | 0.79 | 0.66 | 0.57 |
| $PM_{2.5}$_$NH_4$ | 1.42 | 1.97 | 2.99 | 2.88 | 1.91 | 0.98 | 0.40 | 0.19 | 0.24 | 0.20 | 0.16 | 0.13 |
| $PM_{2.5}$_OM | 5.39 | 0.92 | 2.07 | 2.07 | 0.93 | 1.04 | 2.47 | 0.49 | 0.87 | 0.87 | 0.50 | 0.55 |
| $PM_{2.5}$_EC | 1.08 | 0.52 | 1.12 | 1.13 | 0.52 | 0.58 | 0.32 | 0.27 | 0.49 | 0.49 | 0.27 | 0.30 |
| $PM_{2.5}$_$SO_4$ | 0.87 | 0.53 | 0.82 | 0.81 | 0.53 | 0.46 | 1.04 | 0.54 | 0.61 | 0.60 | 0.53 | 0.49 |
| $PM_{2.5}$_dust | 0.90 | 0.11 | 0.11 | 1.65 | 1.50 | 4.18 | 2.08 | 0.04 | 0.03 | 6.49 | 5.16 | 10.05 |
| $PM_{10}$ | 31.55 | 14.93 | 22.81 | 28.32 | 20.10 | 24.52 | 34.82 | 7.08 | 8.69 | 38.12 | 30.19 | 48.02 |

873

874 Supplementary Table 1. Correlation with surface observations for meteorological variables at
875 Fresno, CA

| | 4km_D2 | 20km_D2 | 20km_P7 |
|---|---|---|---|
| T | 0.94 | 0.94 | 0.94 |
| RH | 0.98 | 0.98 | 0.96 |
| Wind | 0.83 | 0.84 | 0.85 |
| Rain | 0.97 | 0.97 | 0.97 |

876

877 Supplementary Table 2. Bias for surface meteorological variables at Fresno, CA

| | Cold season | | | Warm season | | |
|---|---|---|---|---|---|---|
| | 4km_D2 | 20km_D2 | 20km_P7 | 4km_D2 | 20km_D2 | 20km_P7 |
| T (K) | 3.89 | 3.56 | 3.69 | 2.44 | 1.50 | 1.35 |
| RH (%) | -9.78 | -14.55 | -19.35 | -9.48 | -9.32 | -11.16 |
| Wind (m/s) | -0.67 | -1.00 | -1.05 | 0.78 | -0.16 | -0.49 |
| Rain (mm/day) | -0.15 | 0.14 | -0.03 | -0.06 | -0.03 | -0.04 |

878

# List of Figures

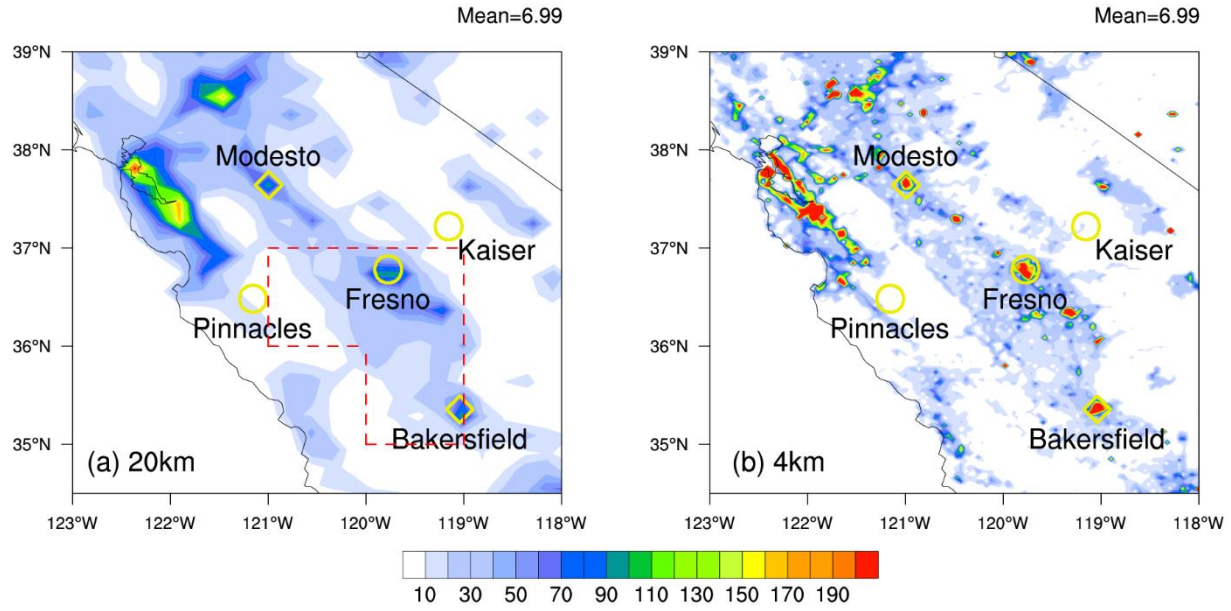


Figure 1. Daily mean anthropogenic $PM_{2.5}$ emission rate (μg $m^{-2}$ $hr^{-1}$) at (a) 20km and (b) 4km simulation. Domain-averaged emission rate is shown at right corner of each figure. Red dashed lines in Figure 1a represent the region used for the domain averages in the discussions. Yellow circle: IMPROVE site; yellow diamond: EPA CSN site. Three urban sites: Fresno, Bakersfield and Modesto; two rural sites: Pinnacles and Kaiser.

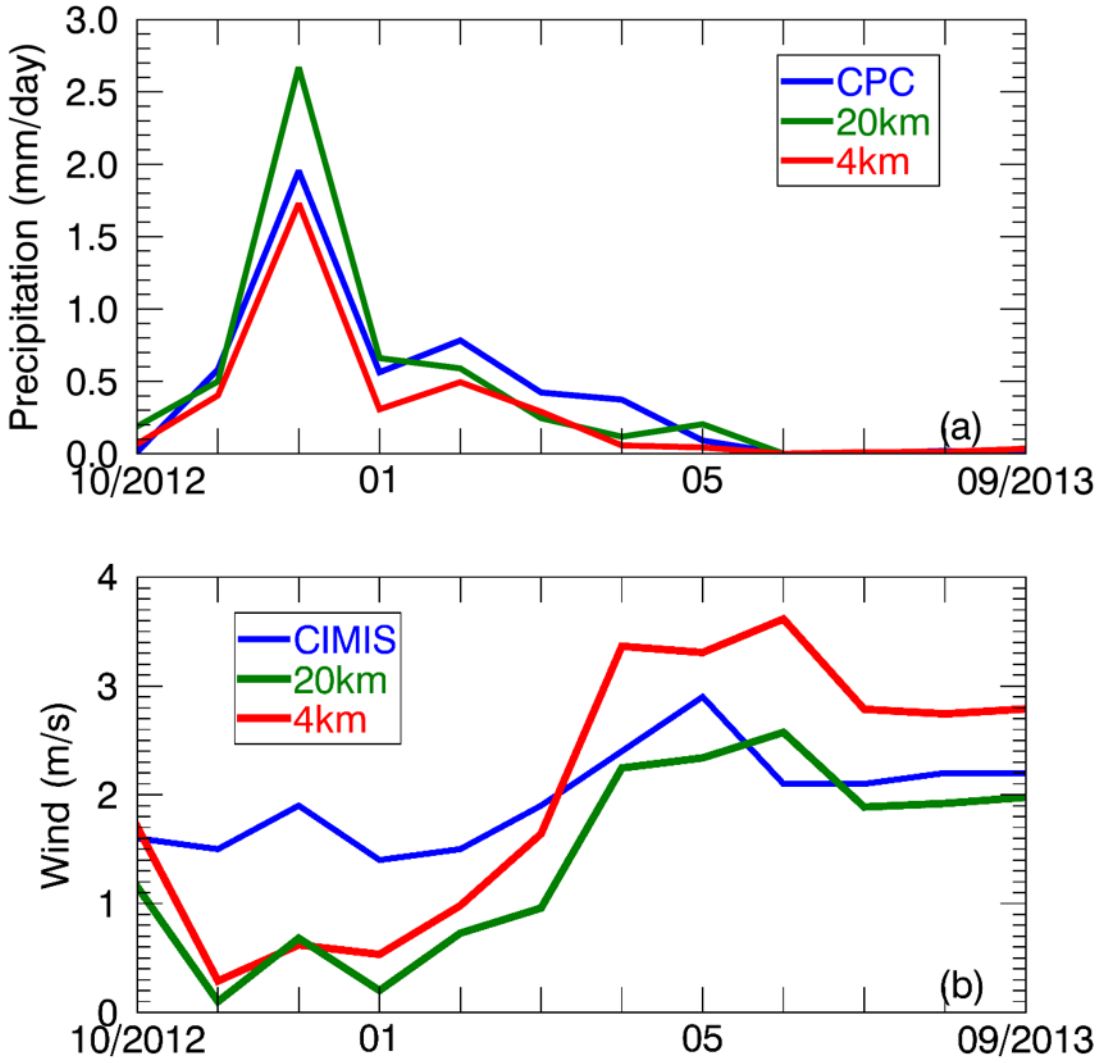


886

887 Figure 2. (a) Monthly precipitation (mm/day) from CPC, 20km and 4km; (b) monthly wind speed
888 (m/s) from CIMIS, 20km and 4km. 4km_D2 (not shown) is similar to 4km.

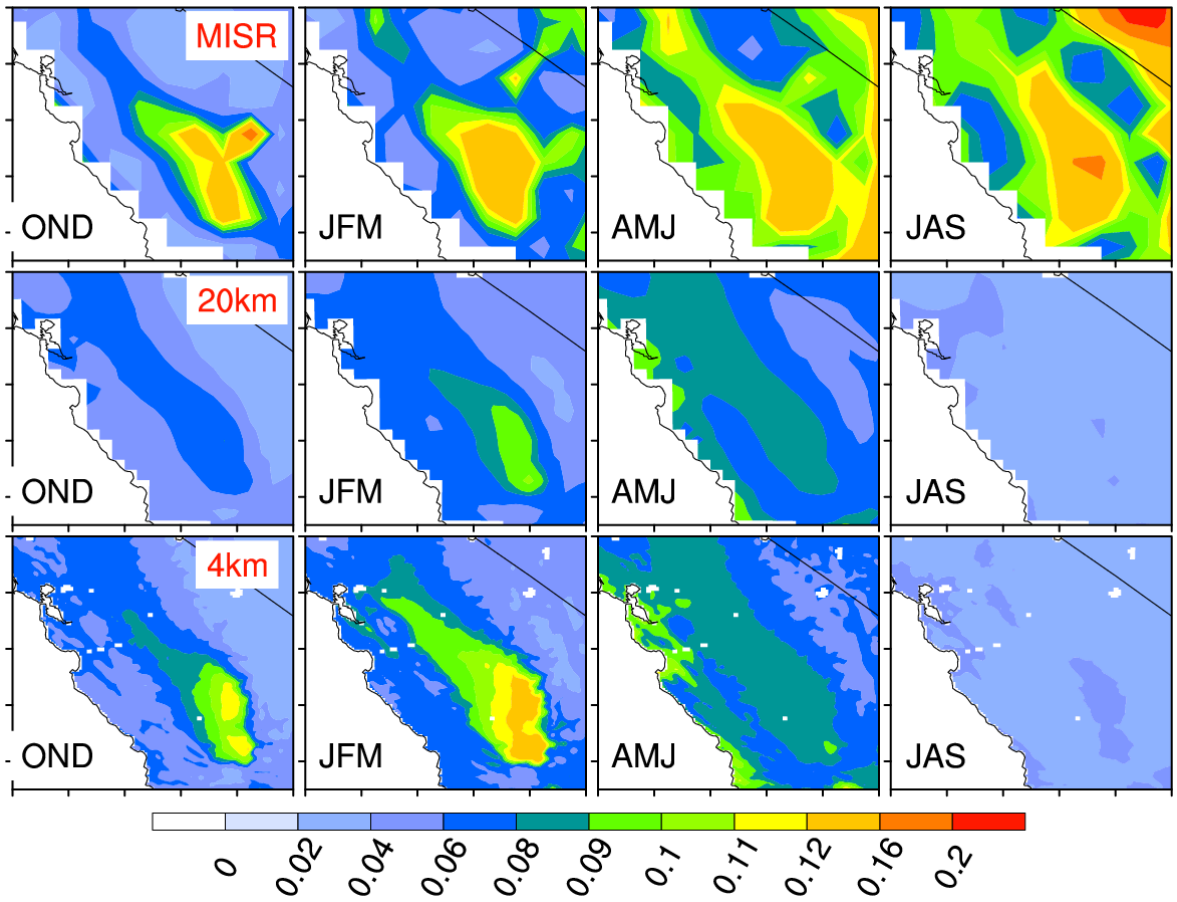


889

890 Figure 3. Spatial distribution of seasonal mean 550 nm AOD from MISR and the WRF-Chem
891 (20km and 4km) simulations in WY2013. OND: October-November-December; JFM: January-
892 February-March; AMJ: April-May-June; JAS: July-August-September.

893

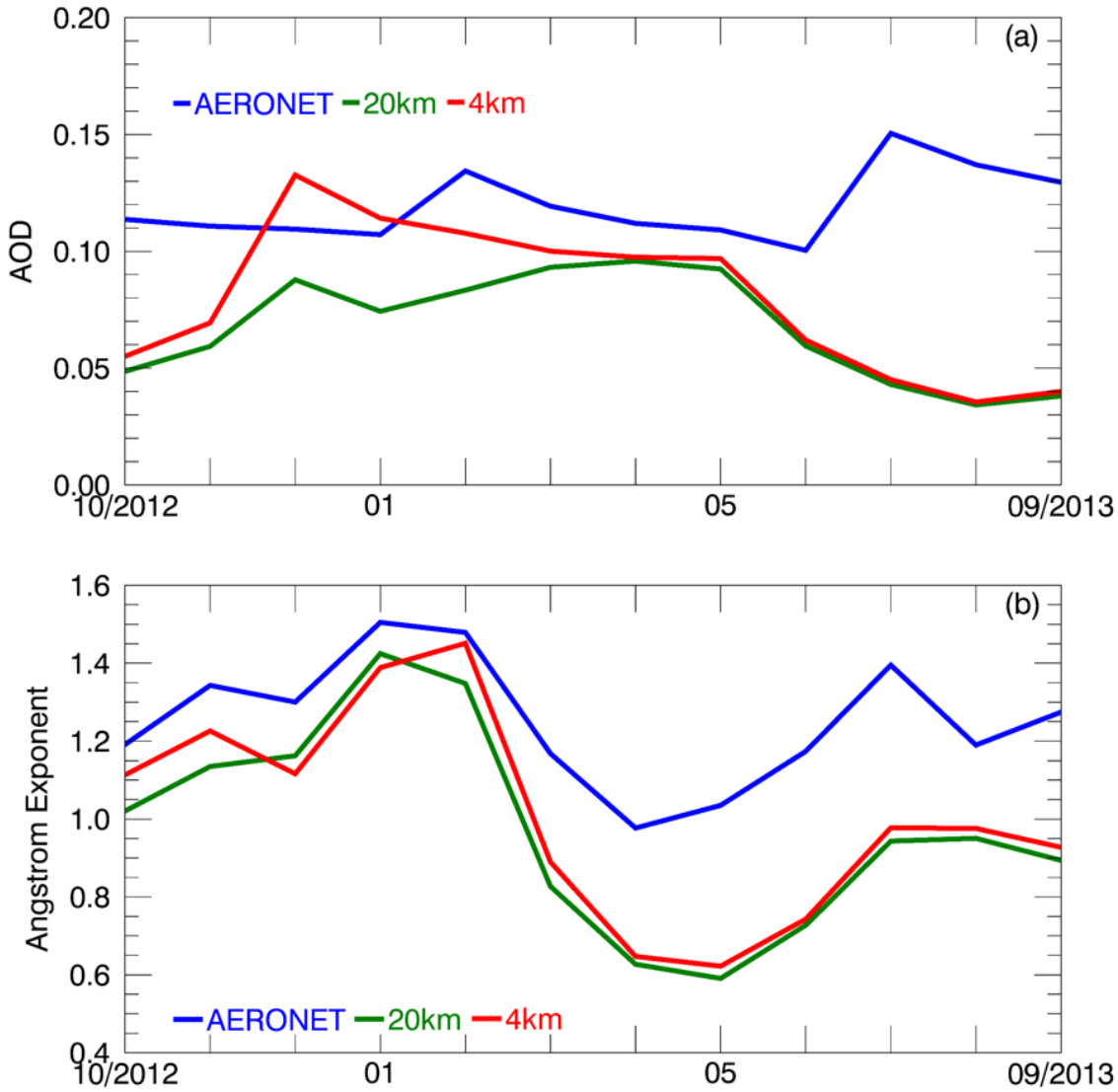


894

895 Figure 4. (a) Monthly mean 550 nm AOD; (b) monthly mean 400-600 nm Ångström exponent at
896 Fresno, CA from October 2012 to September 2013.

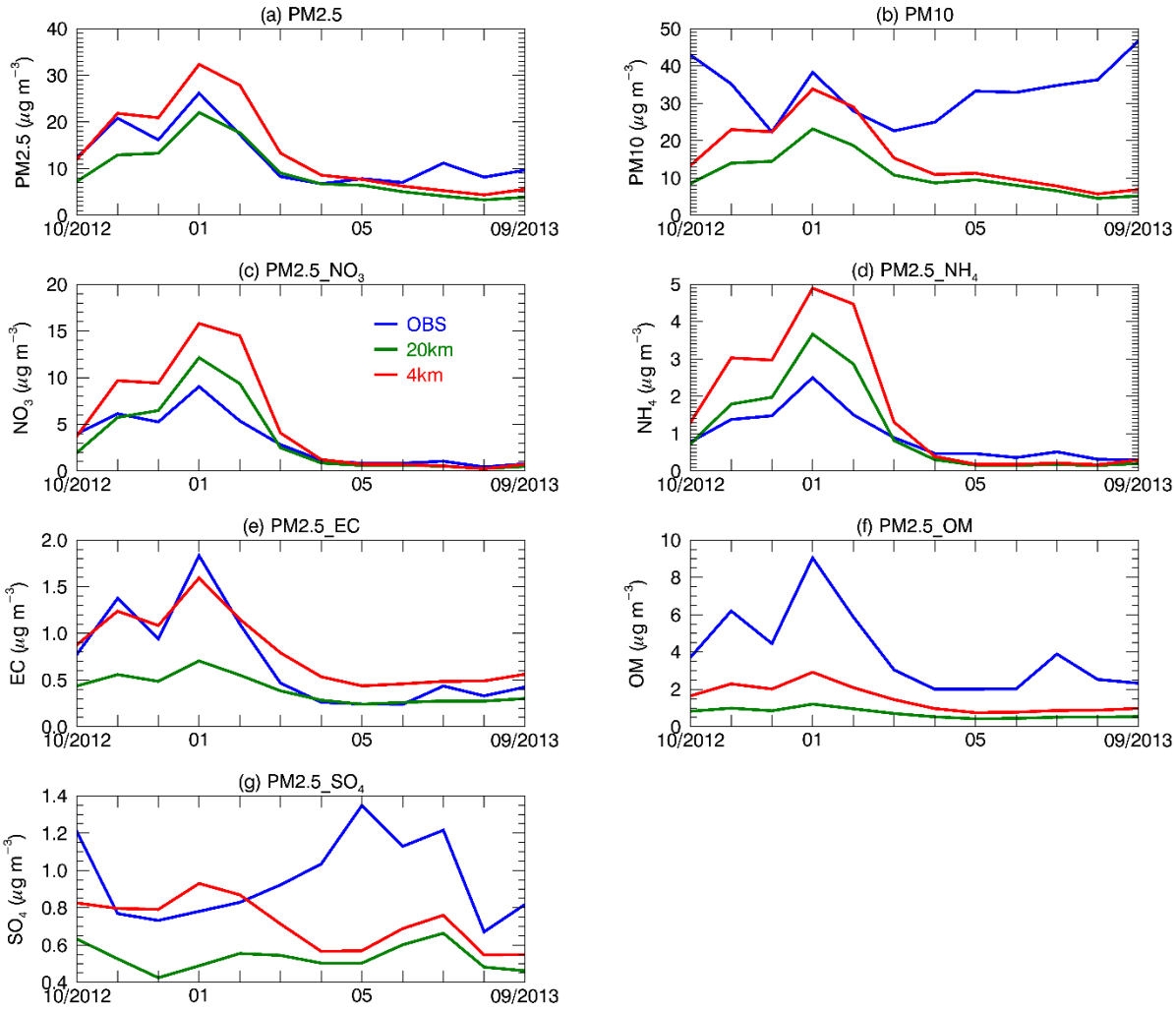


897

898 Figure 5. Aerosol mass (μg $m^{-3}$) for different species from OBS, the 20km and 4km simulations at
899 Fresno, CA. $NH_4$ observations are from EPA; other observations are from IMPROVE. $PM_{2.5}\_NO_3$
900 represents $NO_3$ with diameter $\leq 2.5$ μm. Similar definition for $NH_4$, EC, OM and $SO_4$ in the figures.

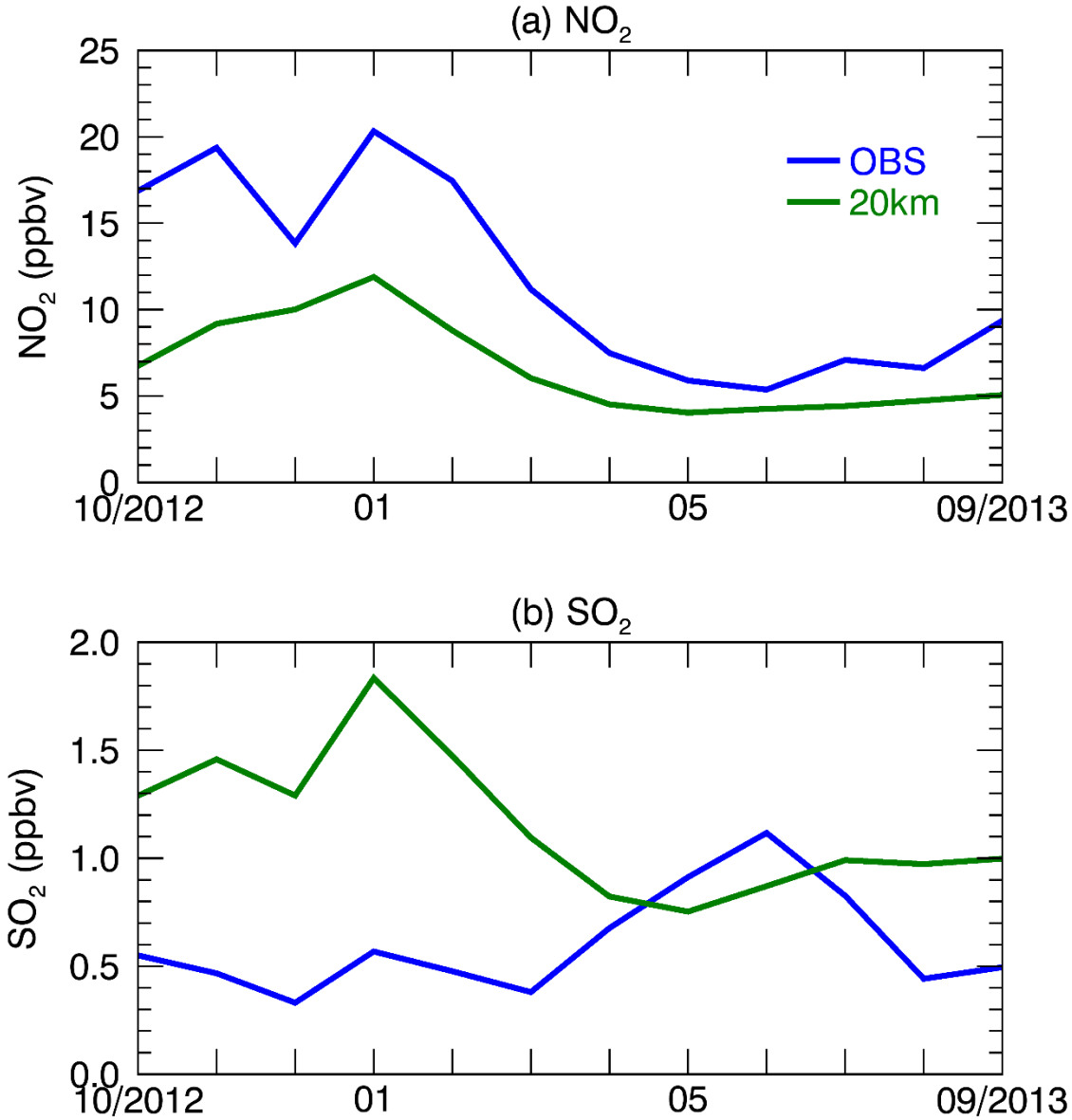


901

902 Figure 6. (a) $NO_2$ and (b) $SO_2$ from EPA (OBS) and the 20km run at Fresno, CA.

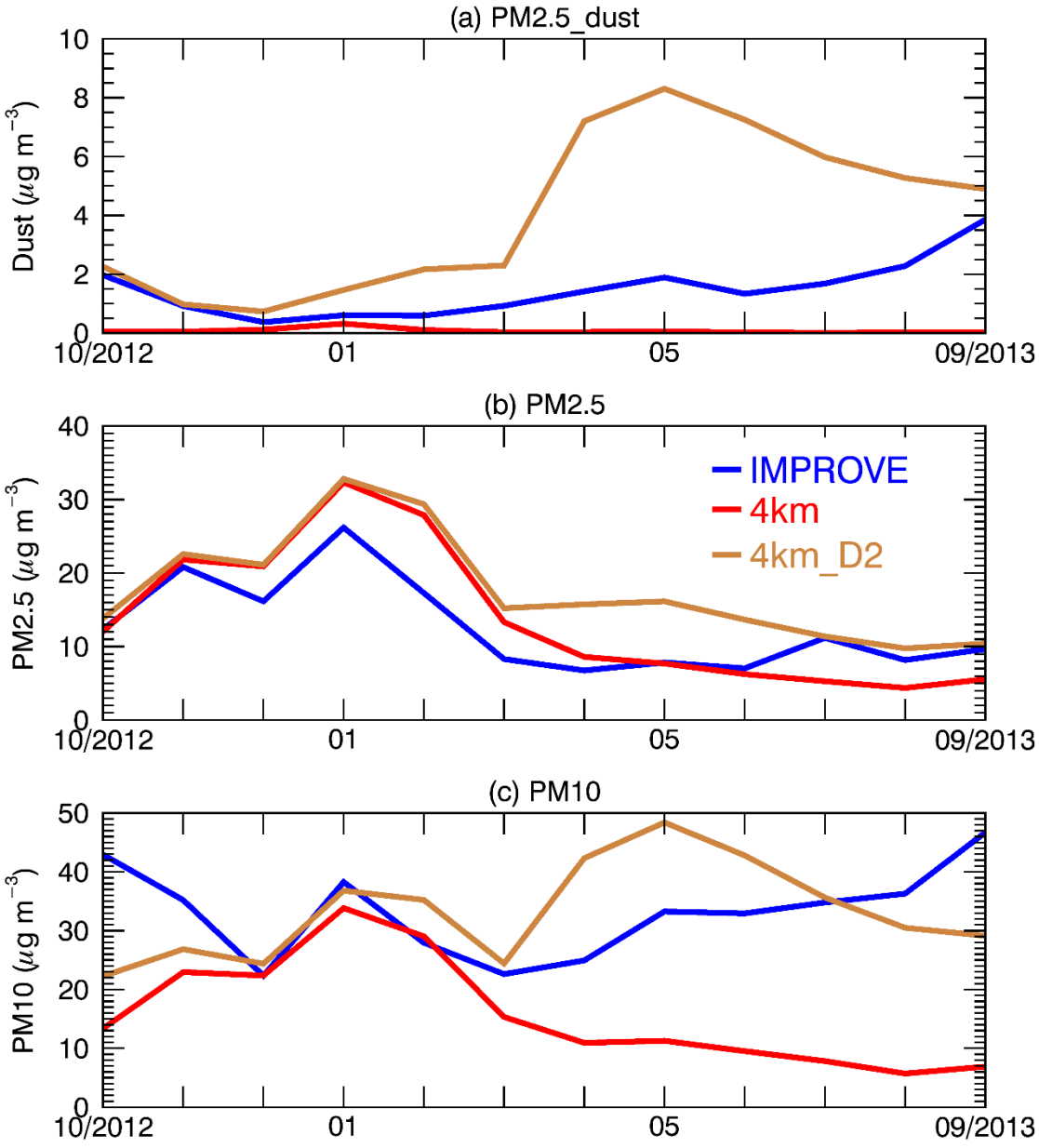


Figure 7. (a) $PM_{2.5}$_dust; (b) $PM_{2.5}$; and (c) $PM_{10}$ from IMPROVE, the 4km and 4km_D2 simulations at Fresno, CA.

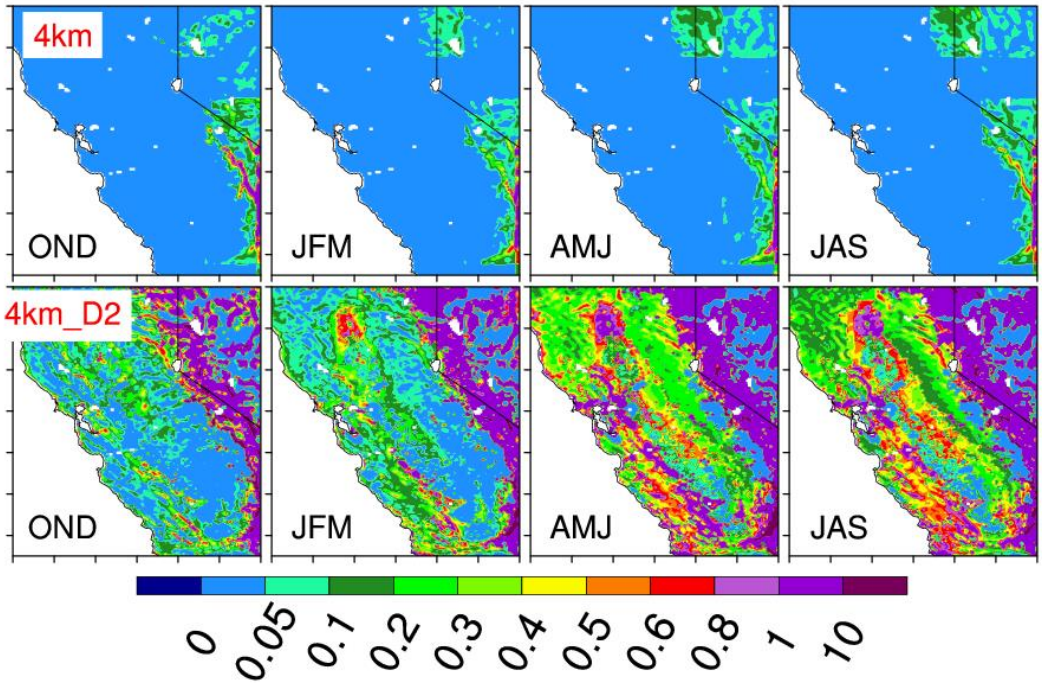


906

907 Figure 8. Mean dust emission rate (μg $m^{-2}$ $s^{-1}$) from the 4km and 4km_D2 runs.

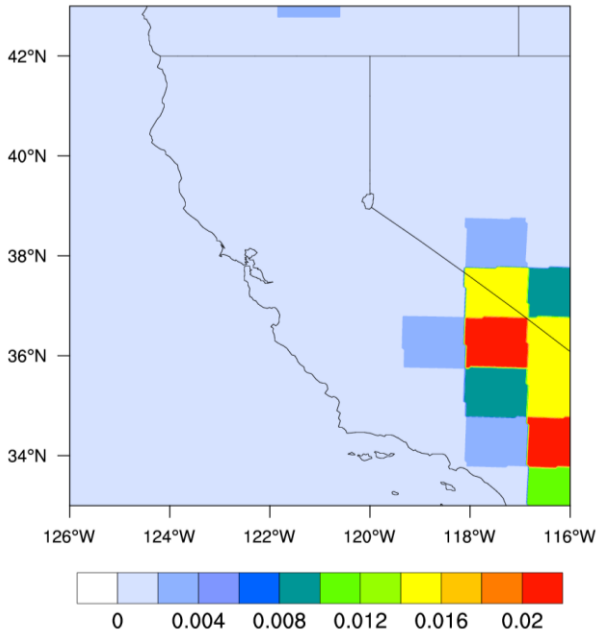


908

909 Figure 9. Fraction of erodible surface in the GOCART dataset used in this study.

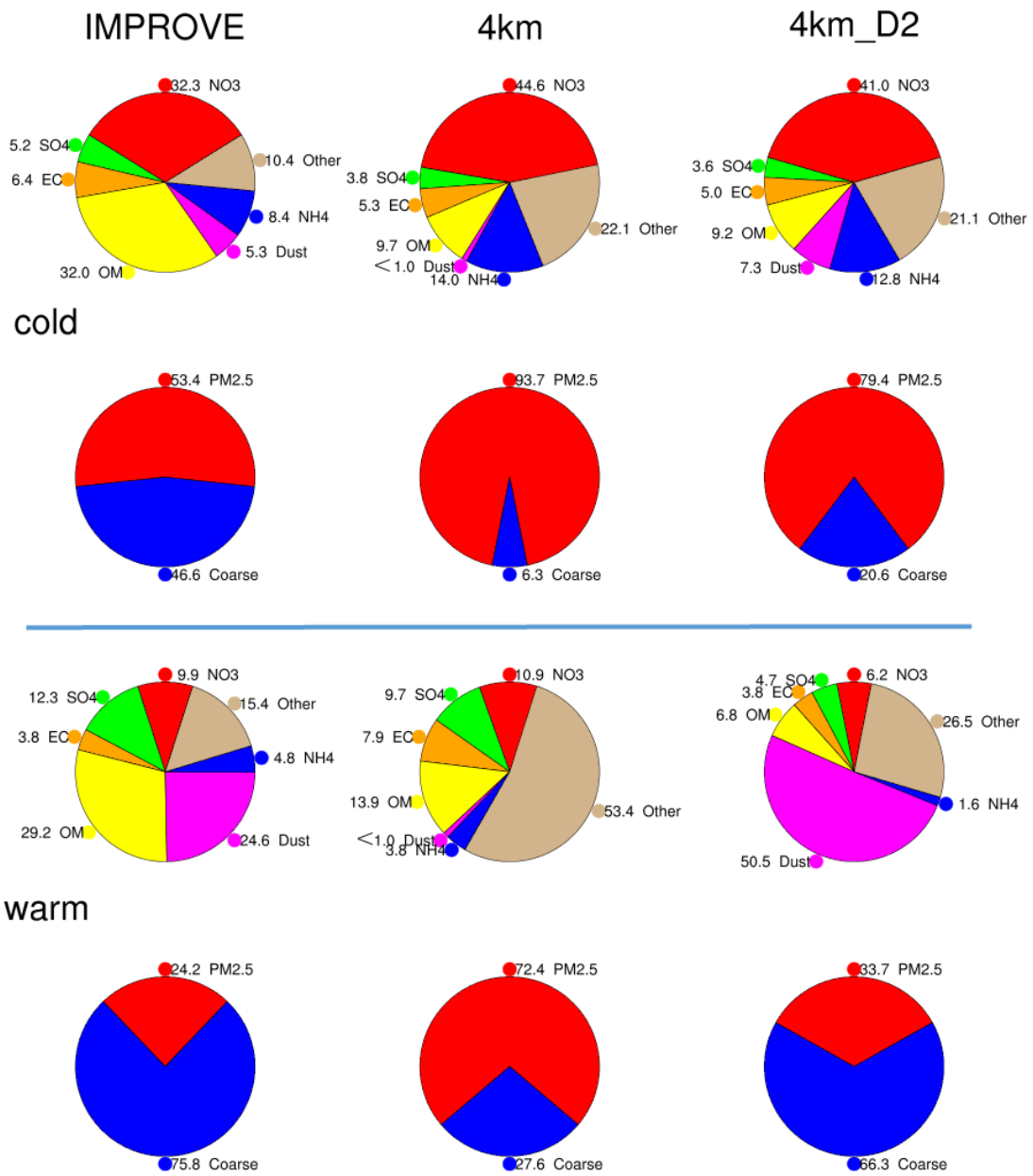


910

911 Figure 10. Relative contribution (%) of aerosol species from IMPROVE and the WRF-Chem (4km
912 and 4km_D2) simulations at Fresno, CA in WY2013. (Panel 1) Contribution to $PM_{2.5}$ in the cold
913 season; (Panel 2) relative contribution of $PM_{2.5}$ and coarse mass (CM) to $PM_{10}$ in the cold season;
914 (Panel 3) same as Panel 1 but in the warm season; (Panel 4) same as Panel 2 but in the warm season.
915 "Other" refers to the difference of $PM_{2.5}$ total mass and specified $PM_{2.5}$ ($NO_3$, $NH_4$, OM, EC, $SO_4$
916 and dust).

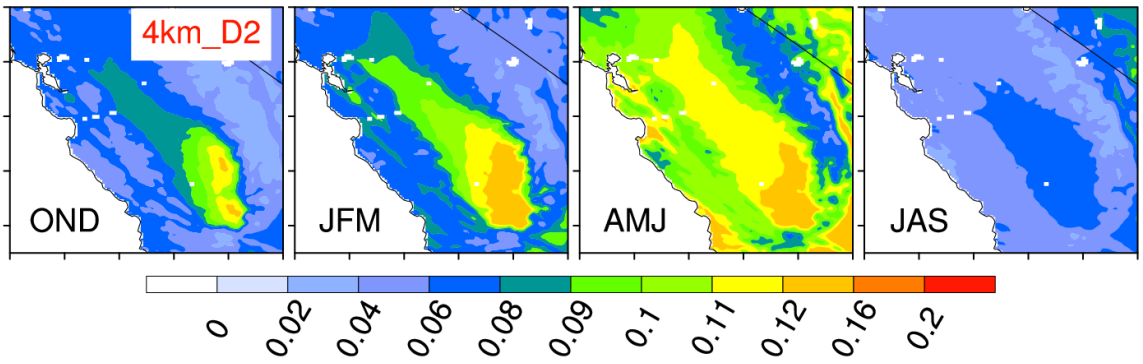


917

918 Figure 11. Spatial distribution of seasonal mean 550 nm AOD from the 4km_D2 run in WY2013.

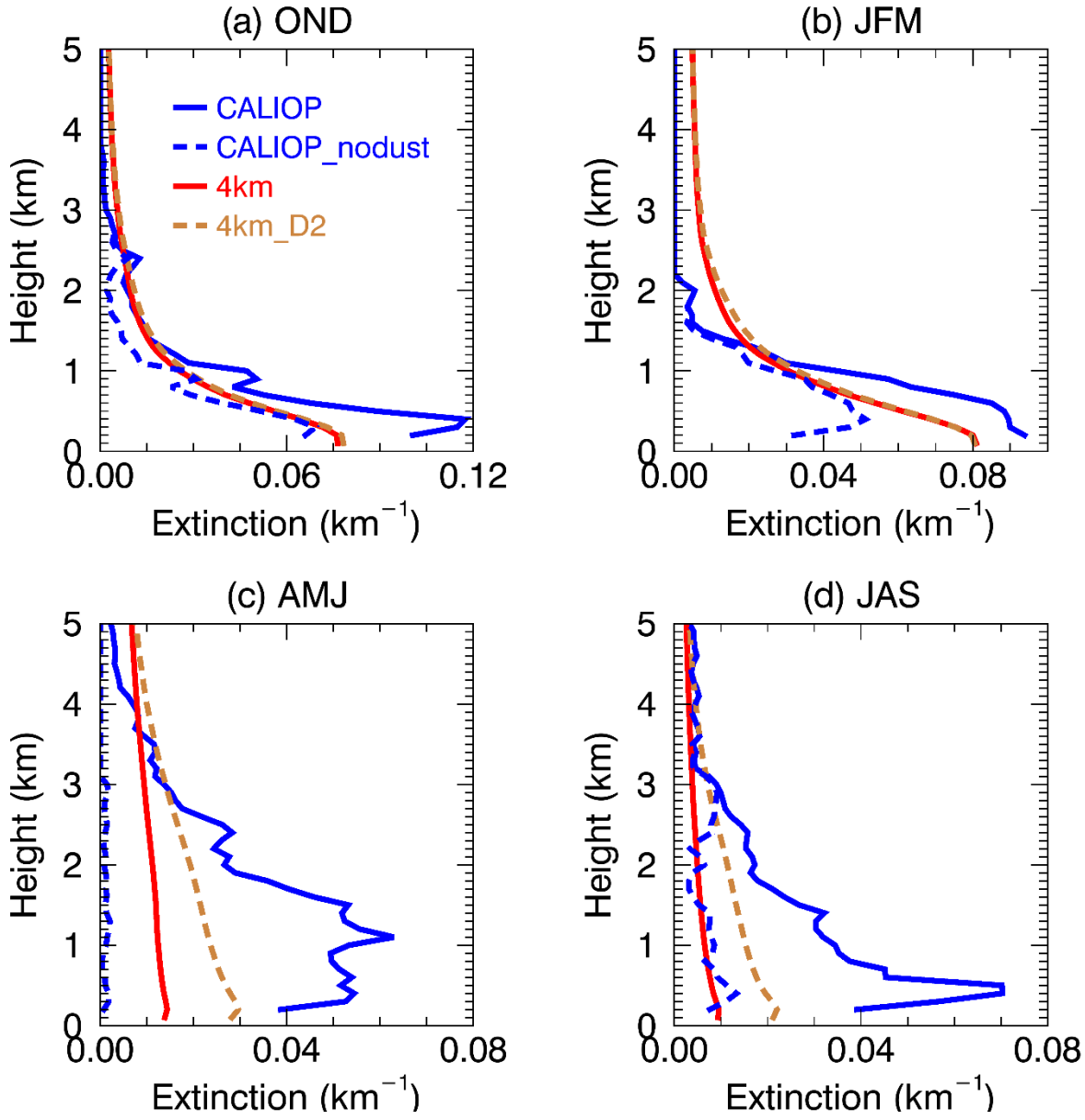


Figure 12. Vertical distribution of seasonal mean 532 nm aerosol extinction coefficient (km$^{-1}$) from CALIOP (blue) and the WRF-Chem (4km and 4km_D2) simulations over the red box region in Fig. 1a in WY2013. Blue dashed lines (CALIOP_nodust) represent the CALIOP profiles without dust (dust and polluted dust).

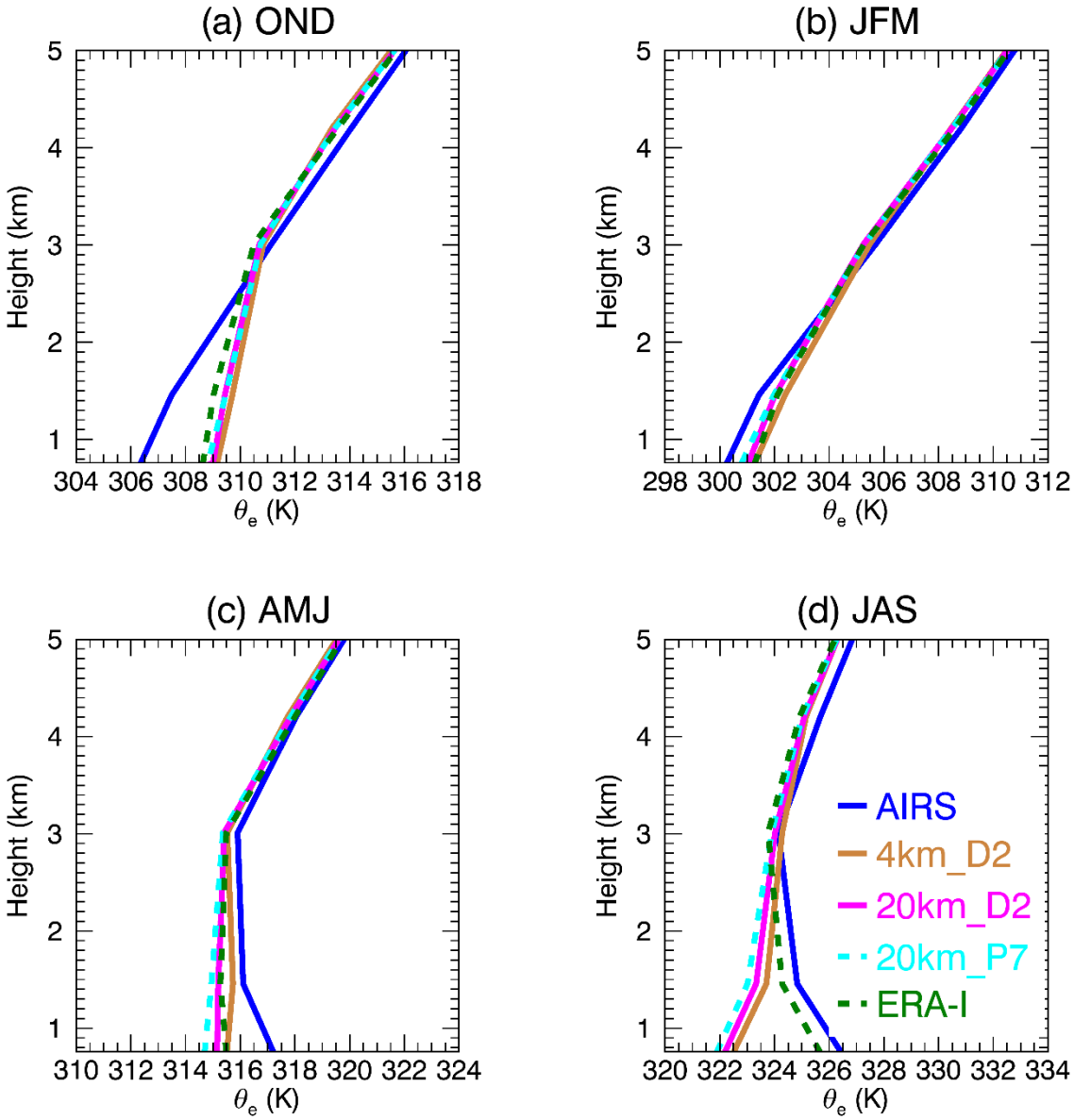


924

925 Figure 13. Vertical distribution of season mean equivalent potential temperature ($\theta_e$; K) from AIRS,
926 ERA-Interim (ERA-I) and the WRF-Chem (4km_D2, 20km_D2 and 20km_P7) simulations over
927 the red box region in Fig. 1a in WY2013. The 4km run (not shown) is similar to the 4km_D2 run.

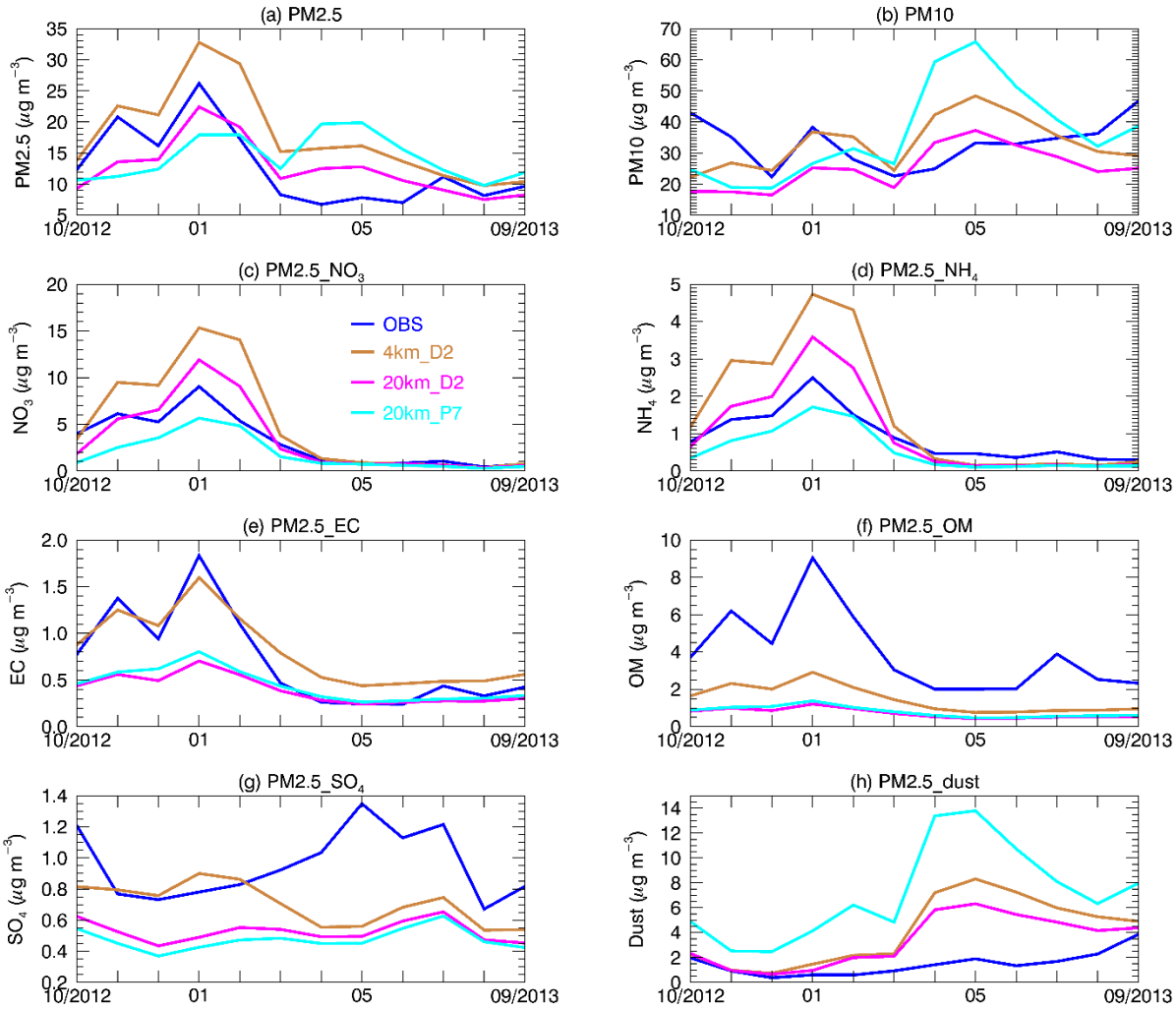


928

929 Figure 14. Aerosol mass (μg $m^{-3}$) for different species from OBS, the 4km_D2, 20km_D2 and
930 20km_P7 simulations at Fresno, CA. $NH_4$ observations are from EPA; other observations are from
931 IMPROVE. $PM_{2.5}\_NO_3$ represents $NO_3$ with diameter ≤ 2.5 μm. Similar definition for $NH_4$, EC,
932 OM, $SO_4$ and dust in the figures.

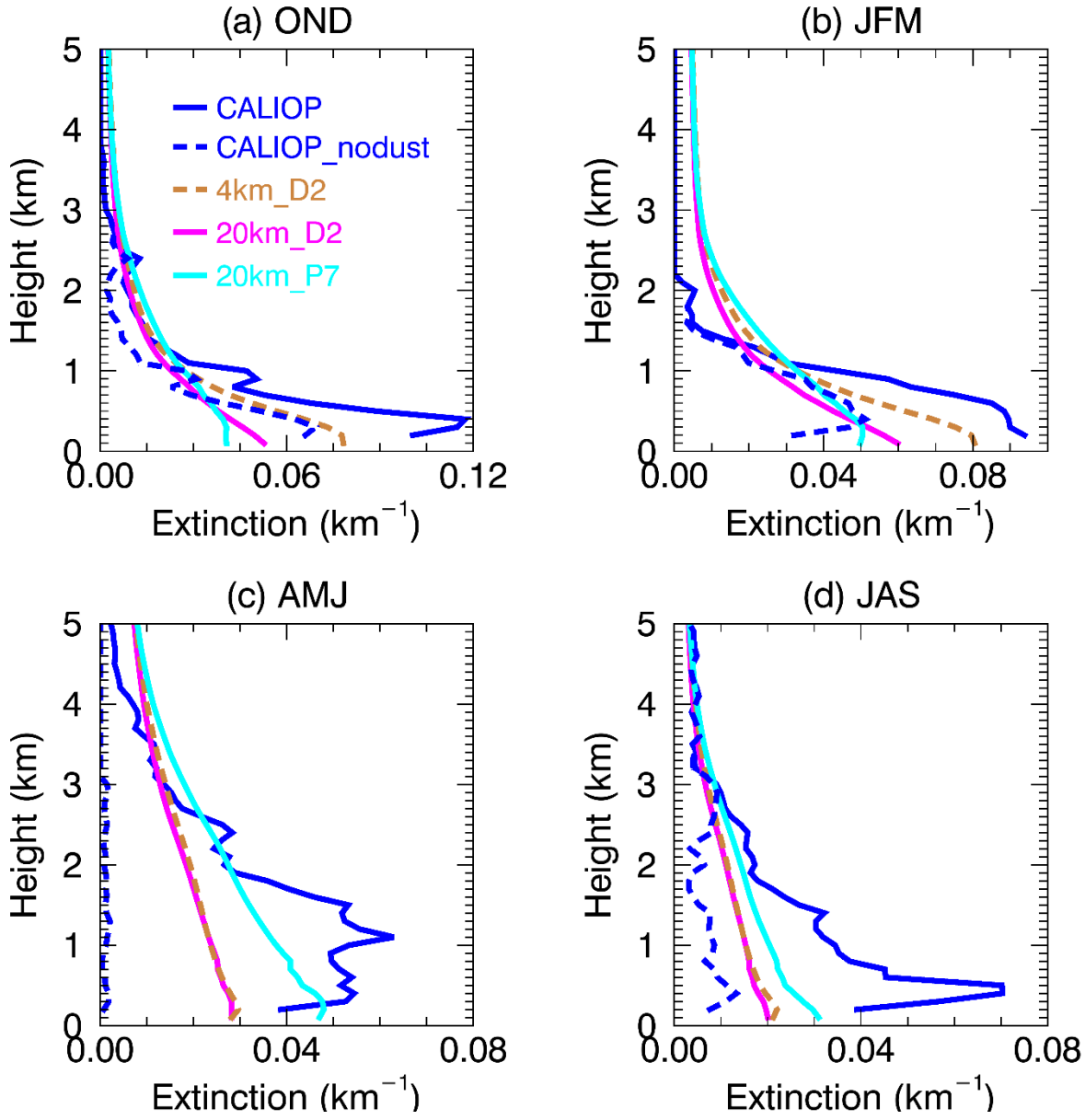


933

934 Figure 15. Vertical distribution of seasonal mean 532 nm aerosol extinction coefficient ($km^{-1}$)
935 from CALIOP, CALIOP_nodust, and the WRF-Chem (4km_D2, 20km_D2 and 20km_P7)
936 simulations over the red box region in Fig. 1a in WY2013.

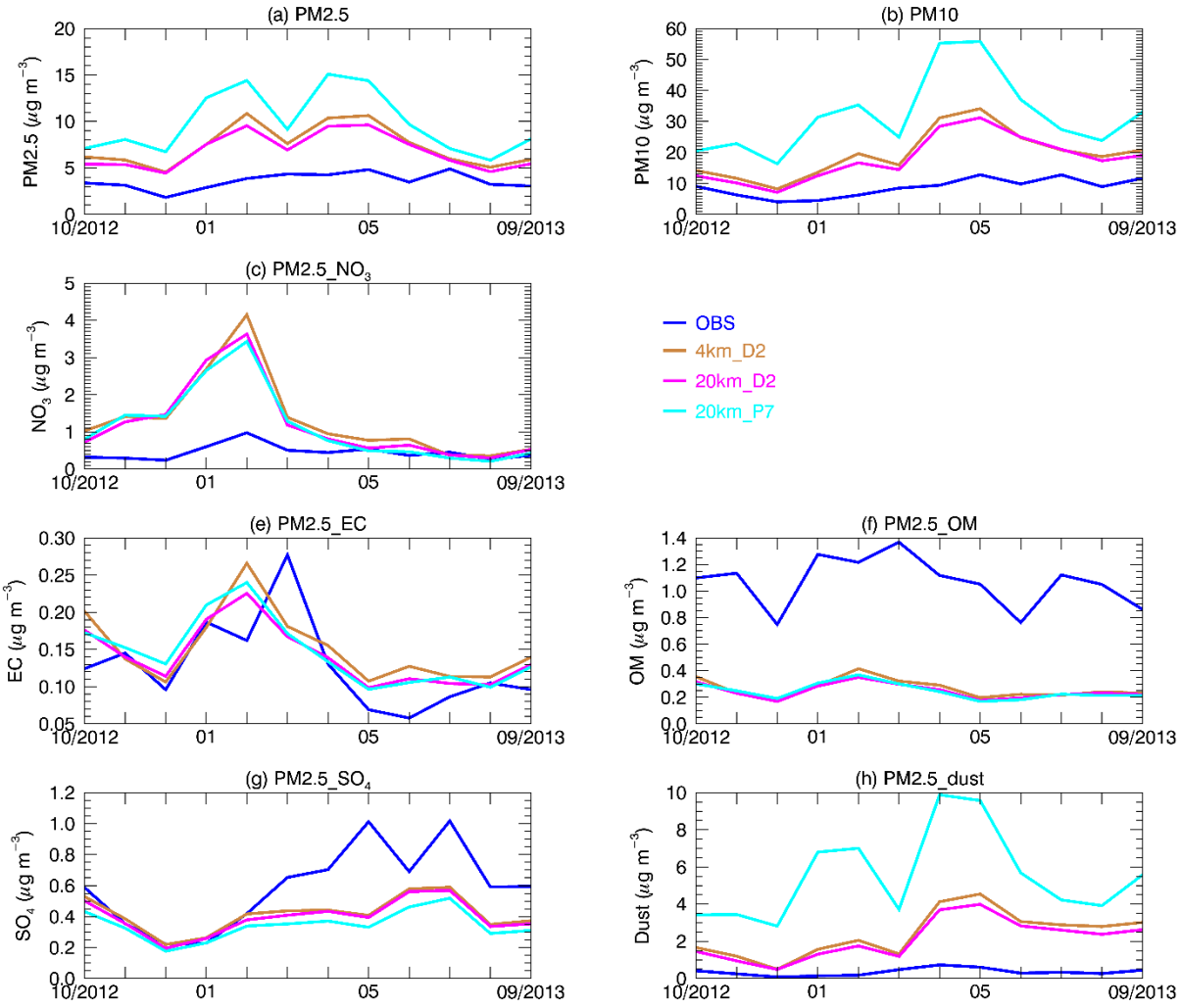


937

938 Figure 16. Aerosol mass (μg $m^{-3}$) for different species from IMPROVE (OBS), the 4km_D2,
939 20km_D2 and 20km_P7 simulations at Pinnacles, CA.

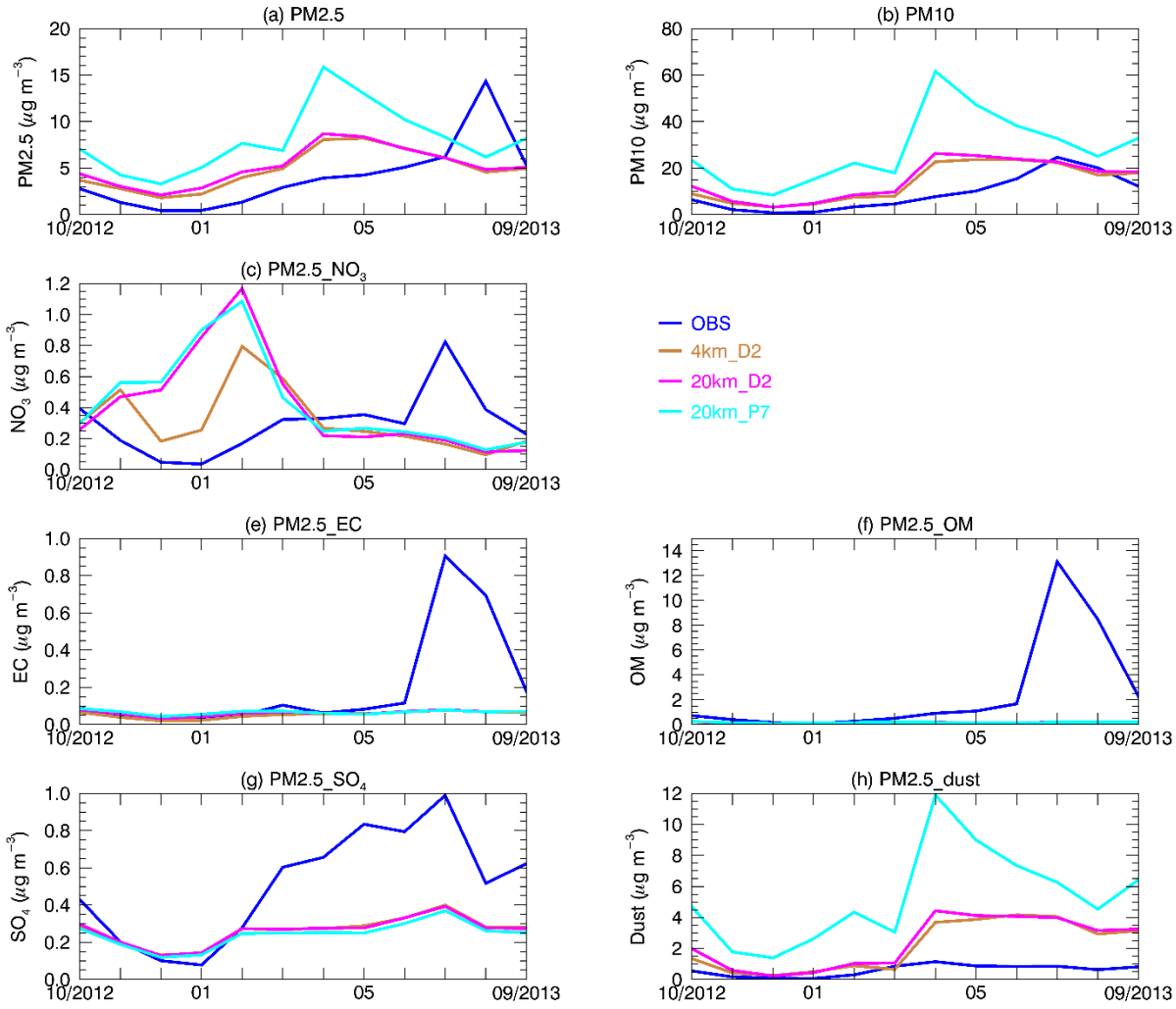


940

941 Figure 17. Aerosol mass (μg $m^{-3}$) for different species from IMPROVE (OBS), the 4km_D2,
942 20km_D2 and 20km_P7 simulations at Kaiser, CA.

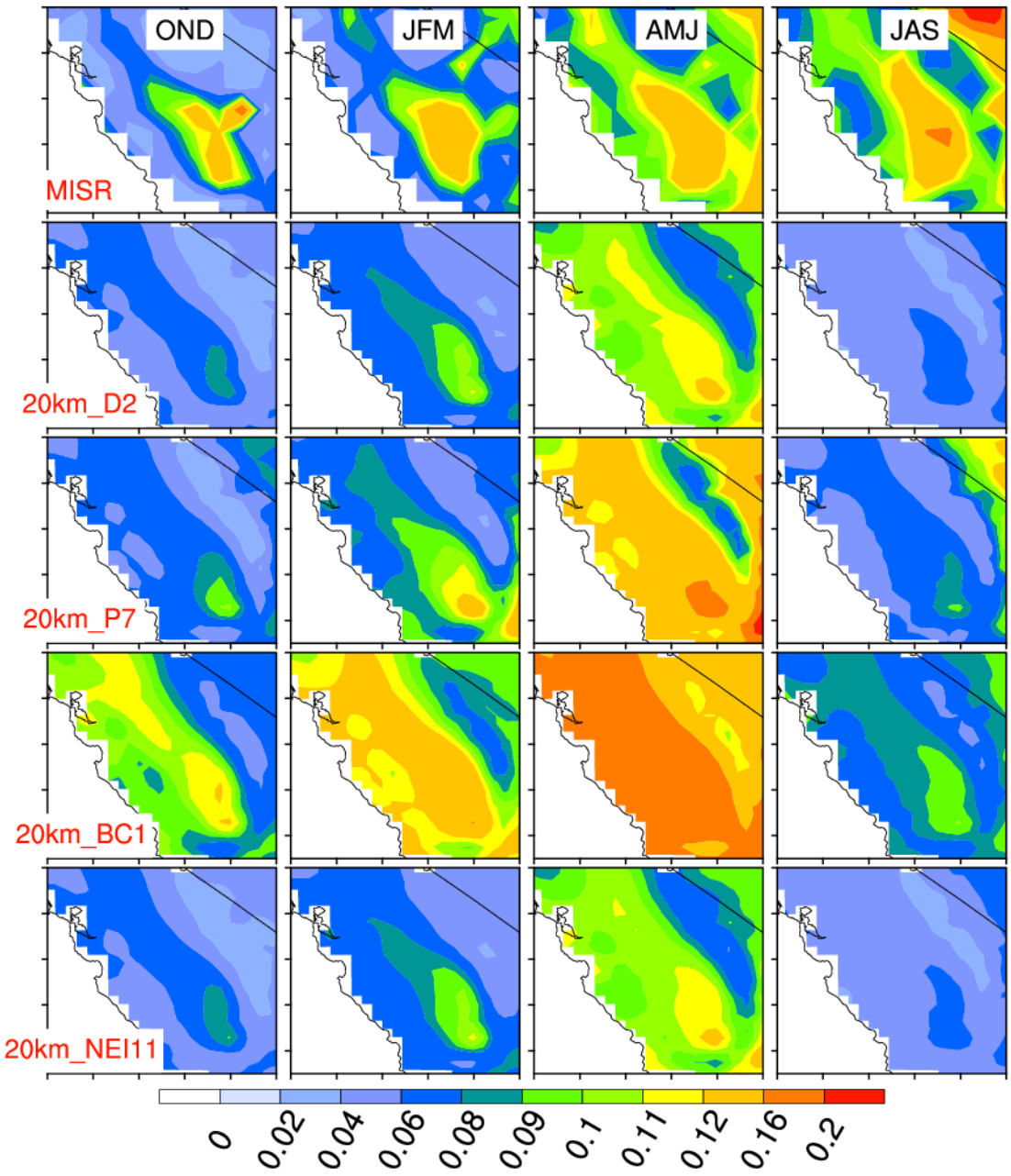


943

944 Supplementary Figure 1. Spatial distribution of seasonal mean 550 nm AOD from MISR and the
945 WRF-Chem (20km_D2, 20km_P7, 20km_BC1 and 20km_NEI11) simulations in WY2013. OND:
946 October-November-December; JFM: January-February-March; AMJ: April-May-June; JAS: July-
947 August-September. The 20km_BC1 run is the same as the 20km_D2 run except that chemical
948 boundary conditions use MOZART-4 original data. The 20km_NEI11 run is the same as the
949 20km_D2 run except with NEI11 anthropogenic emissions.

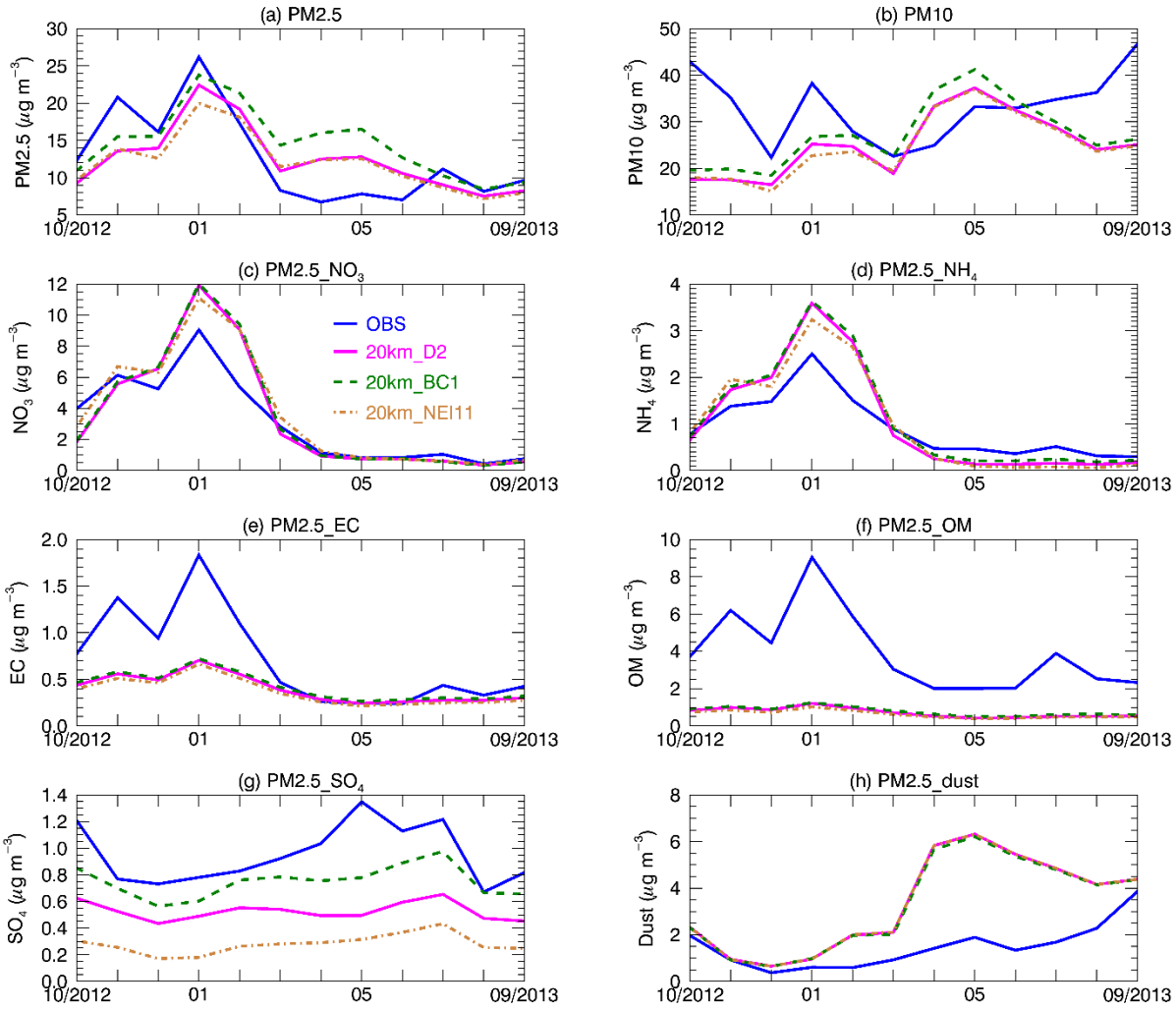


950

951 Supplementary Figure 2. Aerosol mass (μg $m^{-3}$) for different species from OBS, the 20km_D2,
952 20km_BC1 and 20km_NEI11 simulations at Fresno, CA. $NH_4$ observations are from EPA; other
953 observations are from IMPROVE. $PM_{2.5}$_$NO_3$ represents $NO_3$ with diameter ≤ 2.5 μm. Similar
954 definition for $NH_4$, EC, OM, $SO_4$ and dust in the figures.

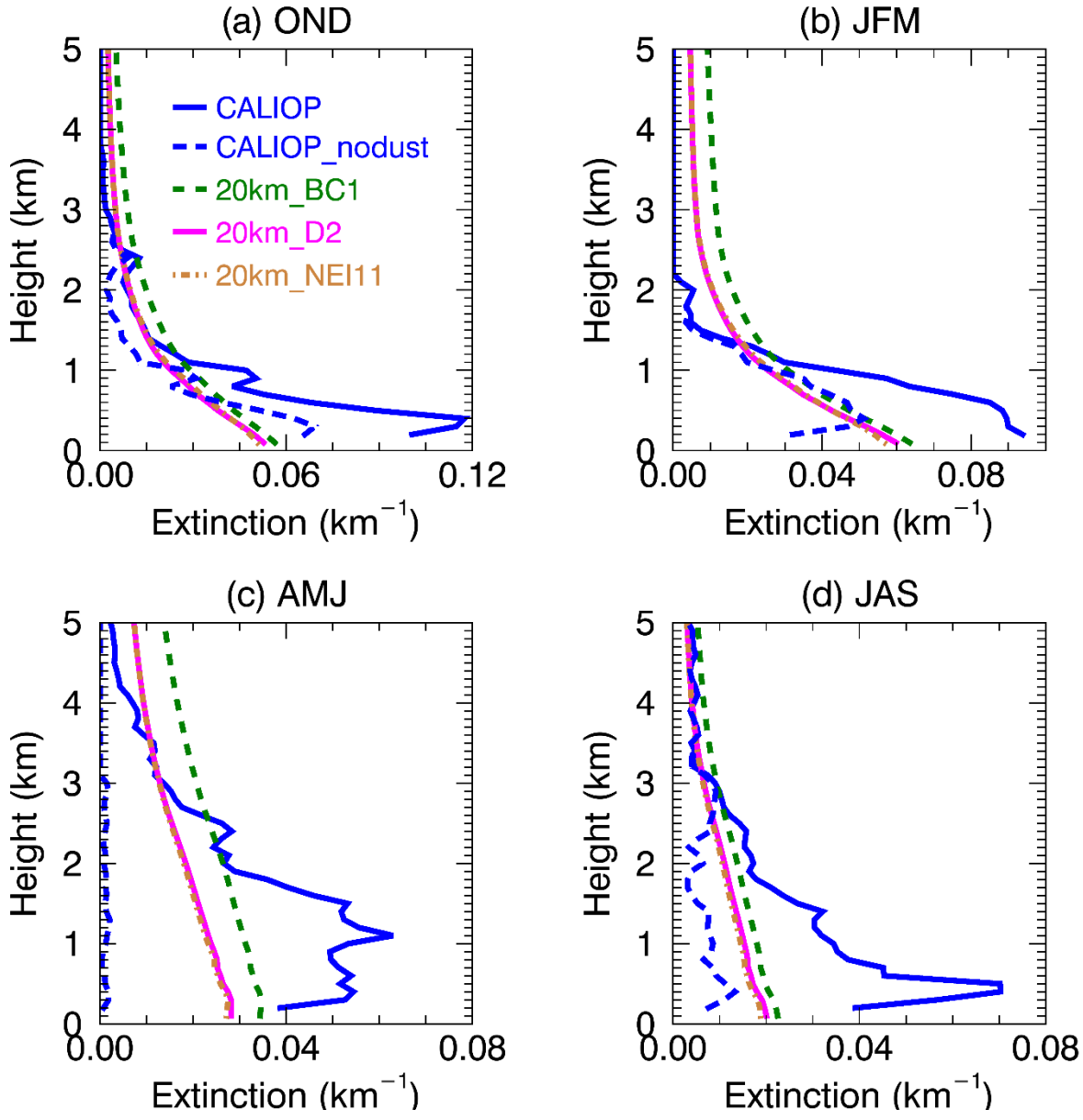


Supplementary Figure 3. Vertical distribution of seasonal mean 532 nm aerosol extinction coefficient (km$^{-1}$) from CALIOP, CALIOP_nodust, and the WRF-Chem (20km_D2, 20km_BC1 and 20km_NEI11) simulations over the red box region in Fig. 1a in WY2013.

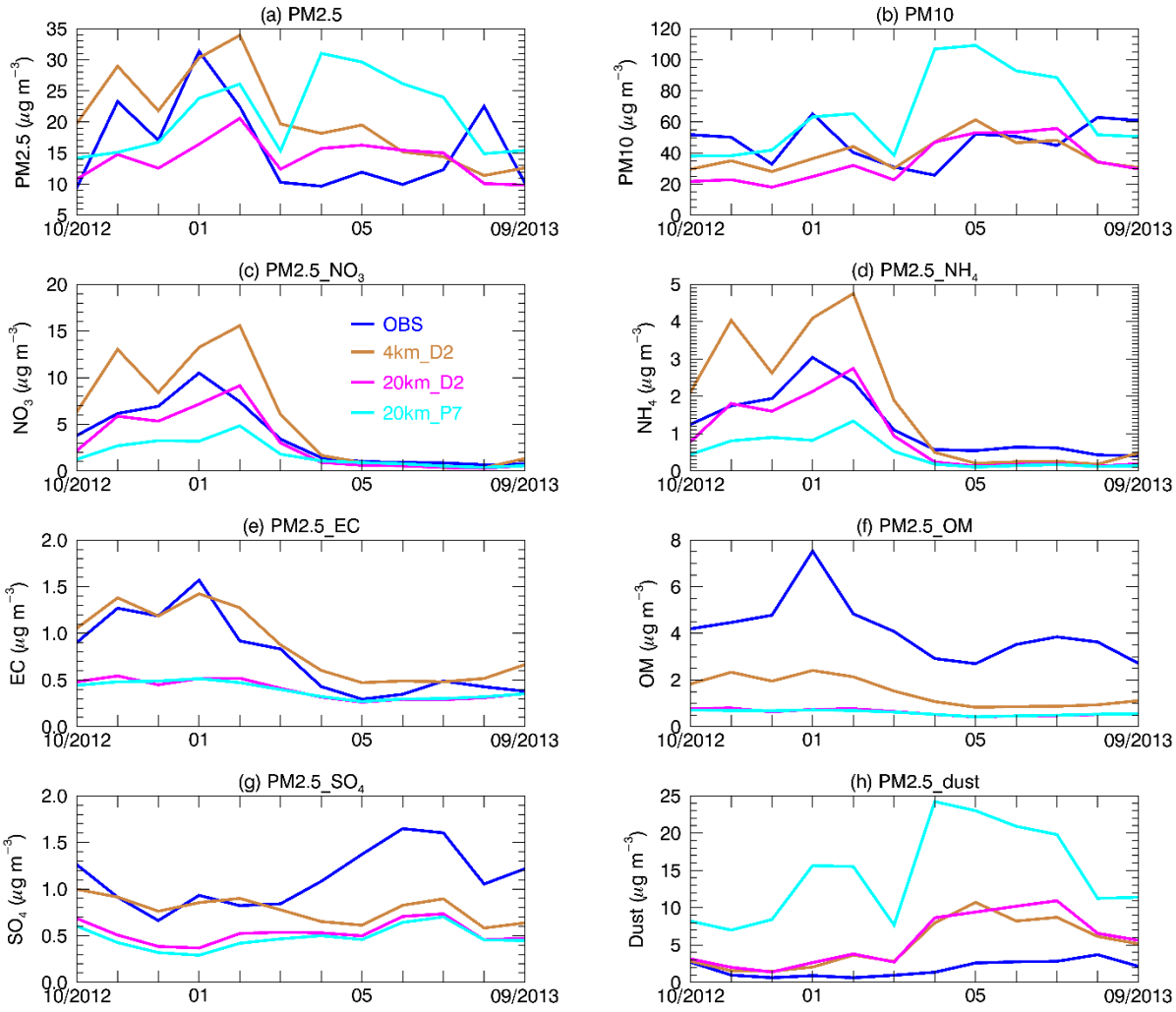


959

960 Supplementary Figure 4. Aerosol mass (μg $m^{-3}$) for different species from EPA CSN (OBS), the
961 4km_D2, 20km_D2 and 20km_P7 simulations at Bakersfield, CA. $PM_{2.5}$_$NO_3$ represents $NO_3$
962 with diameter $\leq$ 2.5 μm. Similar definition for $SO_4$, EC, OM, $NH_4$ and dust in the figures.

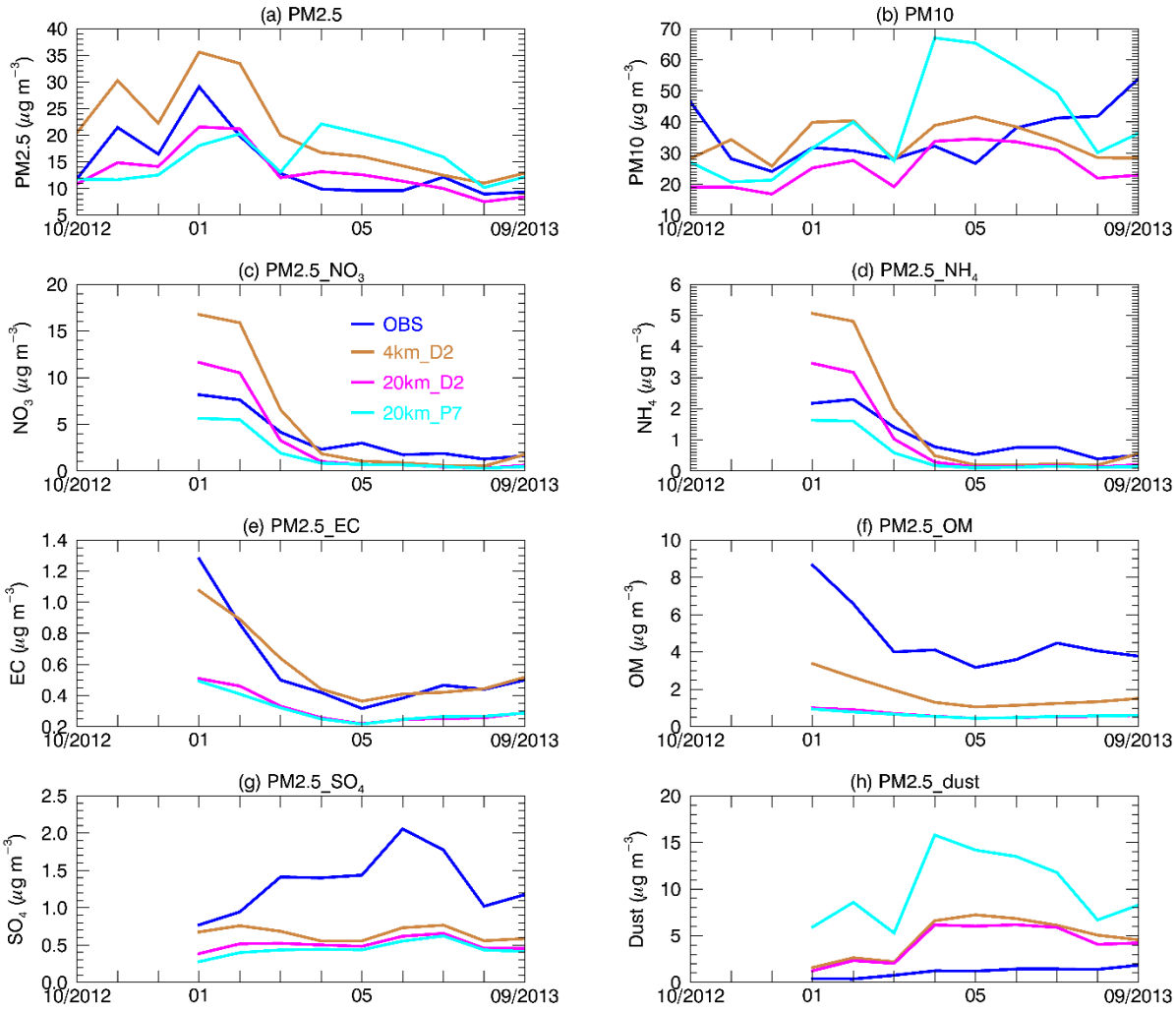


963

964 Supplementary Figure 5. Aerosol mass (μg $m^{-3}$) for different species from EPA CSN (OBS), the
965 4km_D2, 20km_D2 and 20km_P7 simulations at Modesto, CA.

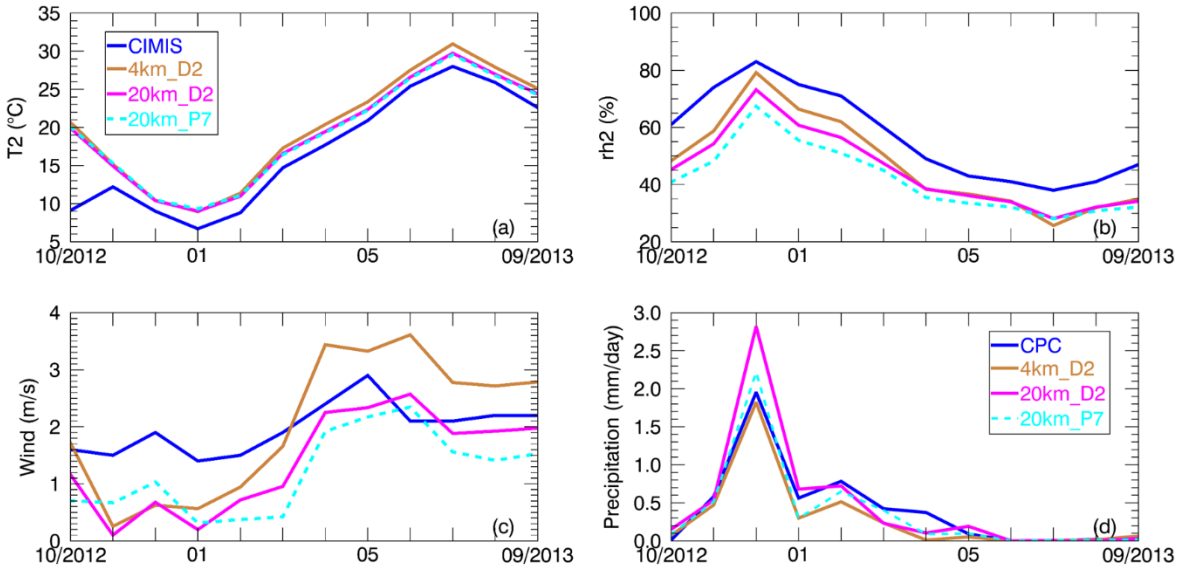


966

967 Supplementary Figure 6. Monthly mean of (a) 2-m temperature (°C); (b) 2-m relative humidity
968 (%); (c) 10-m wind speed (m/s); (d) precipitation (mm/day) at Fresno, CA. The 20km (not shown)
969 run is similar to the 20km_D2 run while the 4km (not shown) run is similar to the 4km_D2 run.

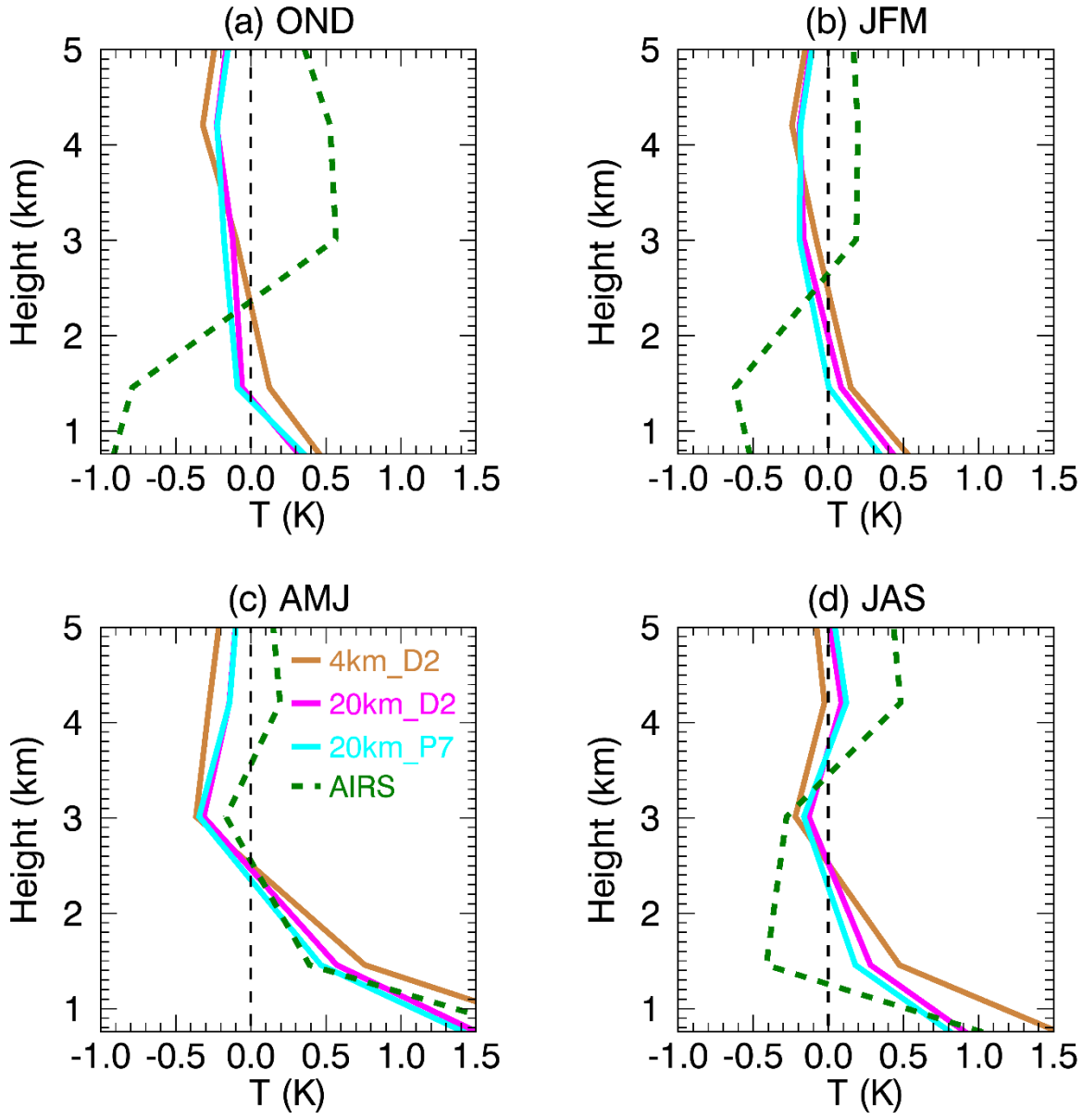


970

971 Supplementary Figure 7. Vertical profile of seasonal mean temperature (K) bias in the WRF-Chem
972 simulations and AIRS comparing to ERA-Interim. The 20km run (not shown) is similar to the
973 20km_D2 run while the 4km run (not shown) is similar to the 4km_D2 run.

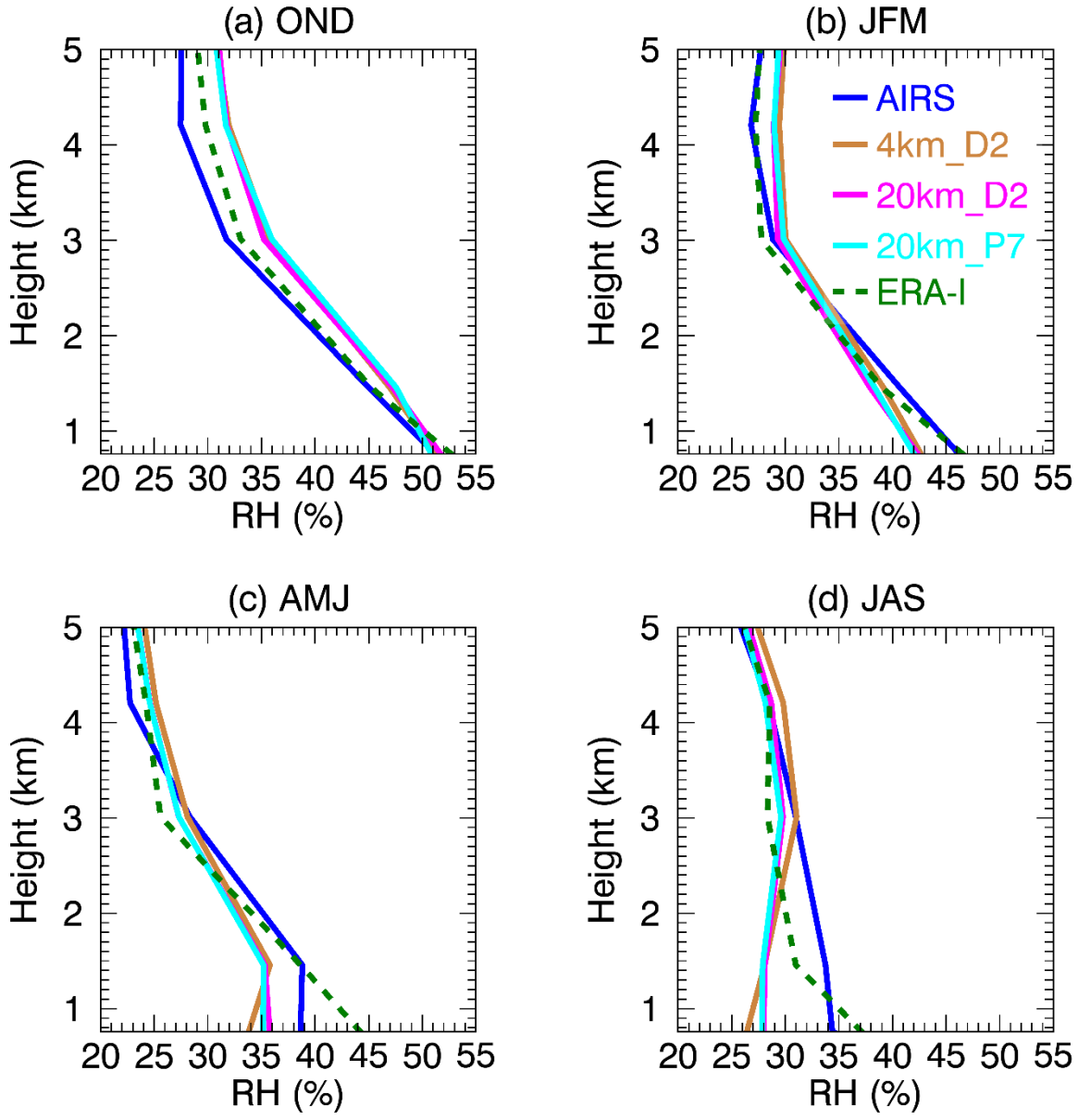


974

975 Supplementary Figure 8. Vertical profile of seasonal mean relative humidity (%) in the WRF-Chem
976 simulations, AIRS and ERA-Interim. The 20km run (not shown) is similar to the 20km_D2 run
977 while the 4km run (not shown) is similar to the 4km_D2 run.

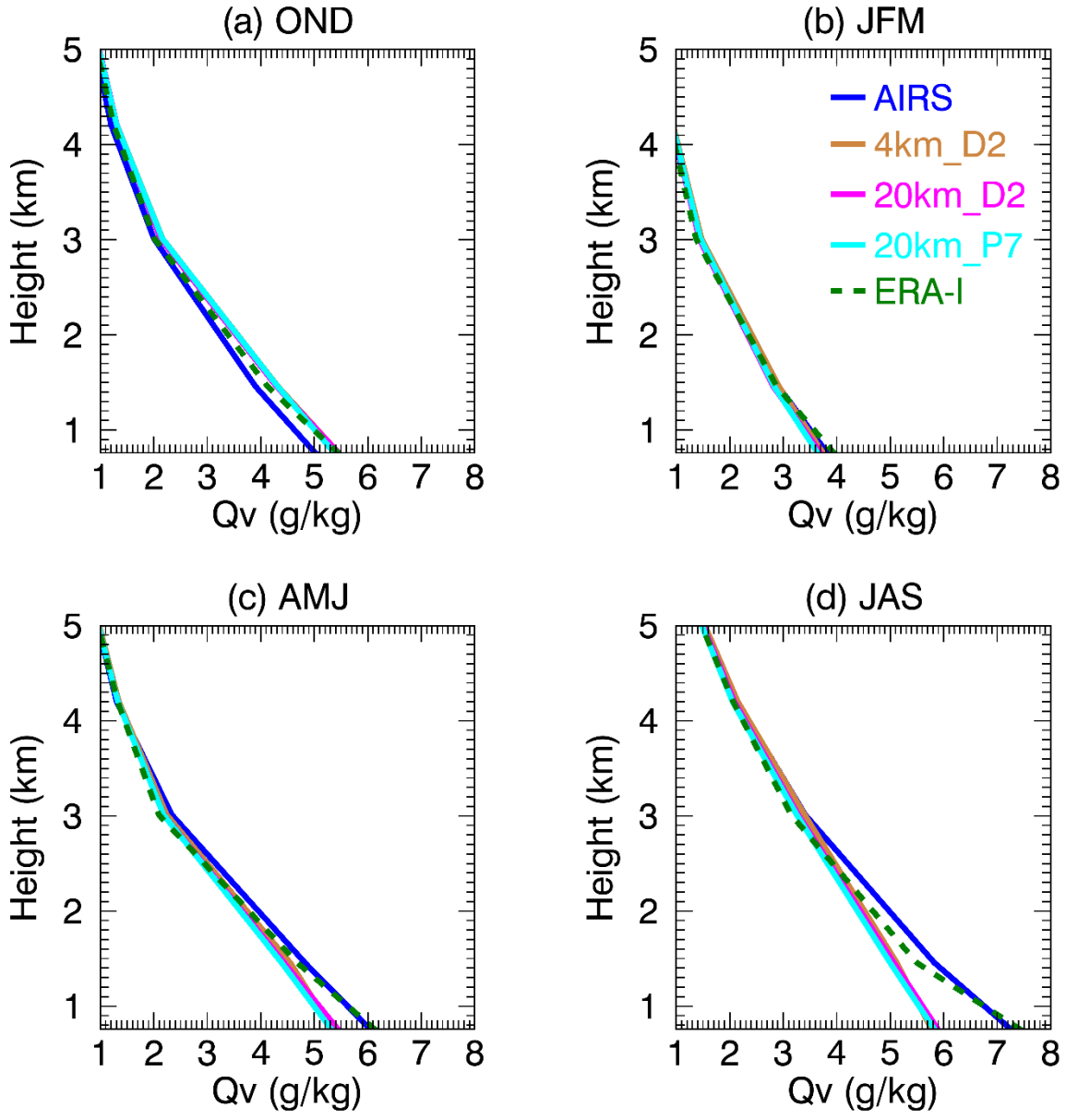


Supplementary Figure 9. Vertical profile of seasonal mean specific humidity (g $kg^{-1}$) in the WRF-Chem simulations, AIRS and ERA-Interim. The 20km run (not shown) is similar to the 20km_D2 run while the 4km run (not shown) is similar to the 4km_D2 run.